

3D NUMERICAL MODELS FOR ALONG-AXIS VARIATIONS IN DIKING AT  
MID-OCEAN RIDGES

by

田小川

(Tian, Xiaochuan)

A Thesis

Submitted in Partial Fulfillment of the  
Requirements for the Degree of  
Master of Science

Major: Geophysics

The University of Memphis

May, 2015

Copyright © 2015 Xiaochuan Tian

All rights reserved

### ***Dedication***

I would like to dedicate this thesis to my mother, Xia Tian. I wouldn't have a chance to experience this wonderful world without her giving birth to me. She rears me up by herself with her great love, optimism and peseverence. Without her guidance and support, I will not become who I am.

I also want to dedicate this thesis toward my major thesis advisor: Dr. Eunseo Choi. His mentorship defines what a great advisor is like. Without his guidance, neither this theis nor my fast personal-development during these two years is possible. He has kindled a flame that illuminates the way for my future career as a geodynamic modeler.

## *Acknowledgements*

There is no proper words for me to express my deep gratitude toward my thesis advisor Dr. Eunseo Choi. He has changed my life in a very positive way. From him, I have learned what a great researcher and educator should be like. It is because of his unfailing care and understanding that have given me the courage to persevere, to carry on during the darkest days as an international student far away from home. It is his vivid and interesting lessons that have inspired me so much that I want to devote my career into geodynamic modeling. It is his numerous inspiration and encouragement that has motivated me to work super hard (enjoy at the same time) on the fascinating research questions. It is his altruistic share that has provided me with great chances to learn from great researchers, references, and to attend meetings. It is his patience to guide me through my endless silly questions that has nourished and cultivated my capabilities of being an independent researcher. Blessings from Eunseo, my role model, are countless. I will keep them in mind and try my best to relay the torch.

To the other two committee members, Dr. Christine Powell and Dr. Jer-ming Chiu, for their guidance and advice during many committee meetings. For their interesting courses.

To Center for Earthquake Research and Information and University of Memphis, thank a lot for providing me this great chance to study here with full tuition and graduate research assistanship. It is this kind support that has made my two year studies at this great institution possible. To all the faculties taught me courses and staff Josephine provided me a very pleasant, tidy and clean place for doing research and studying.

To students, Yangyang Naeem Sabber

To Center for Writing and Communication staff: Bill Schraufnagel To Tianhe2 super computer center, thank a lot for the support from National Supercomputer Center in Guangzhou. For about 200k Sus.

To Dr. Jie Liu and Dr. Ke Zhang, for kindly sharing their computing resources on Tianhe2.

To Dr. Gu Cheng,

To Shengfang Chen and Lijie Lyu

Finally, I want to thank my families, grandfather, grandgrandfather(ling zhong qian rang wo hao hao xue xi), grandma, mum.

“In the midst of winter, I found there was, within me, an invincible summer.”

—Albert Camus

“People have no higher calling than to strive for the greater good of humankind and society and that the future of humanity can be assured only when there is a balance between scientific development and the enrichment of the human spirit.”

—Kazuo Inamori

“不失其所者久，死而不亡者寿。”

—《道德经》

### *Abstract*

Tian, Xiaochuan. M.S. The University of Memphis. May 2015 Master of Science.  
3D Numerical Models for Along-axis Variations in Diking at Mid-Ocean Ridges. Major  
Professor: Dr. Eunseo Choi.

Bathymetry of ocean floors reveals a great variety of morphologies at Mid-ocean Ridges (MORs). Previous studies showed that the morphologies at slow spreading MORs are mainly controlled by the ratio between rates of magma supply and plate extension. 2D models for the across-ridge cross-sections have been successful in explaining many of the observed morphological features such as abyssal hills and oceanic core complexes. However, the magma supply varies along the ridge and the interaction between the tectonic plates and magmatism at MORs are inevitably 3D processes. We propose to investigate the consequences of the along-axis variability in diking in terms of faulting pattern and the associated structures. This work will include implementation of an algorithm of parameterizing repeated diking in a 3D parallel geodynamic modeling code.

## *Table of Contents*

Chapter	Page
<b>1 Introduction</b>	<b>1</b>
1.1 Review of Literature . . . . .	1
1.2 Statement of Research Purpose . . . . .	5
<b>2 Methods</b>	<b>7</b>
2.1 Method of approach . . . . .	7
2.2 Model Setup . . . . .	8
2.3 Parameters to control . . . . .	9
<b>3 Results</b>	<b>14</b>
3.1 Reference model M28LinT1 . . . . .	14
3.1.1 Constant M model M88ConT2 . . . . .	18
3.2 Main characteristics of the models . . . . .	19
3.2.1 Location of <sup>EC:</sup> <u>termination</u> [I think “fault trace” is what you mean.] . . . . .	20
3.2.2 Geometry of axial trough . . . . .	21
3.2.3 Inward fault jump . . . . .	21
3.2.4 Fault alternation . . . . .	21
3.2.5 Cut-back . . . . .	22
3.2.6 Hourglass-shaped median valley . . . . .	24
3.2.7 Corrugations and mullion structures . . . . .	27
3.3 Effects of the functional forms of M variation . . . . .	29
3.3.1 M28(Lin, Sin, Sqrt)T1 . . . . .	29
3.3.2 M58(Lin,Sin,Sqrt)T2 . . . . .	32
3.4 Effects of the weakening rate . . . . .	33
3.4.1 M57SinT1 versus M57SinT2 . . . . .	33

3.4.2	M58SinT1 versus M58SinT2 . . . . .	36
3.4.3	M58SqrtT1 versus M58SqrtT2 . . . . .	40
3.5	Effects of the range of M variation . . . . .	42
3.5.1	(M28 M57 M58)SinT1 . . . . .	43
3.5.2	M57SinT2 versus M58SinT2 . . . . .	44
3.5.3	M28LinT1 versus M57LinT1 . . . . .	44
3.5.4	M28SqrtT1 versus M58SqrtT1 . . . . .	46
3.5.5	M57SqrtT2 versus M58SqrtT2 . . . . .	46
<b>4</b>	<b>Discussion</b> . . . . .	<b>48</b>
4.1	Summary of Results . . . . .	48
4.2	Fault Alternation . . . . .	50
4.2.1	Trade-off between bending and weakening . . . . .	50
4.2.2	Alternating on conjugate plate . . . . .	52
4.2.3	Secondary near-axis normal fault . . . . .	52
4.2.4	Effect of along ridge-axis coupling . . . . .	52
4.3	Corrugations . . . . .	53
4.3.1	Wavelength of corrugations . . . . .	53
4.4	Influence of healing . . . . .	53
4.5	Comparing model results with nature observation . . . . .	53
4.5.1	Cut back at 13°N Mid-Atlantic Ridge (M28SqrtT1) . . . . .	53
4.5.2	Double dome at 23°N Mid-Atlantic Ridge (Kane Megamullions) (Several models) . . . . .	54
4.5.3	Atlantis Massif Shape at 30°N Mid-Atlantic Ridge () . . . . .	54
4.5.4	Shear low . . . . .	54
4.5.5	Corrugations . . . . .	54
4.6	Model Limitation . . . . .	54
4.6.1	Fixed thermal structure effects and justification . . . . .	54

4.7	Recommendation for Future Research . . . . .	55
<b>5</b>	<b>Conclusions</b>	<b>56</b>
	<b>Bibliography</b>	<b>57</b>

*List of Tables*

1	Summary of 3D Model Parameters . . . . .	12
2	List of 3D numerical experiments. . . . .	13
3	Average M values of the 20 km segment. (The value is calculated by integrating M along the ridge axis and divided by the length of the model domain in z-axis.) . . . . .	32
4	Model behaviors in short. . . . .	48
5	Linear functional form. . . . .	48
6	Sinusoidal functional form. . . . .	49
7	Square root functional form. . . . .	49

## *List of Figures*

1	Profiles of bathymetry across MORs. . . . .	2
2	Two bathymetric profiles across the Mid-Atlantic Ridge around 30°N with vertical exaggeration of 10. A-A' is closer to the segment center while B-B' is at the tip of the segment. . . . .	2
3	Relationship between the maximum crustal thickness variations ( $\Delta H_c$ ) along a ridge segment and the segment length (L). The dashed line is the best-fit linear regression of the combined data. [Chen and Lin, 1999] . . . . .	3
4	Upper one: modeling result for fast spreading agrees well with the observation of East Pacific Rise. Lower one: modeling result for slow spreading ridges agrees well with the bathymetry of Mid Atlantic Ridge. [Buck et al., 2005] . . . . .	5
5	Snapshots of modeled fault behavior and seafloor morphology for values M = 0, 0.5, and 0.7; model allows thermal evolution. Structural interpretation is superimposed on modeled distribution of strain rate; model time is indicated in panels at lower right; dashed white line at bottom is 600 °C isotherm and approximates the brittle-ductile transition; dashed seafloor is original model seafloor, red seafloor is that formed dominantly by magmatic accretion, and solid bold seafloor is fault surface.[Tucholke et al., 2008, Whitney et al., 2012]	6
6	Essential components of the numerical method. . . . .	8
7	Model setup . . . . .	9
8	Evolution of plastic strain and surface topography of the reference model M28LinT1 (Table 2). Each snapshot shows plastic strain plotted on the model domain and the five times exaggerated topography. Initial seafloor is marked as a reference of 0 km of the topography. The bold dash lines (black) are the terminations of the detachment faults. The bold dash lines (red) in g) and h) are the transfer faults that connect the terminations along the ridge. The inset in f) plots plastic strain with opacity linearly proportional to its value. . . . .	14

9	Bird's-eye view of the evolution of breakaway (marked by green bold line) and depressed narrow zone ("axial trough") along the ridge axis (red dash line in (a)) for model M28LinT1 (Table 2). This figure share the same color scales with Figure 8. . . . .	15
10	Bending stress illustration. The blue line is the neutral plane where $\sigma_{xx} = 0$ . Above the neutral plane is compression ( $\sigma_{xx} < 0$ ) and beneath it is tension ( $\sigma_{xx} > 0$ ). . . . .	16
11	Bird's-eye view of velocity field with plastic strain plotted with <sup>EC:</sup> <u>opacity</u> [why do you need transparency in this figure?] <sup>XT:</sup> <u>if not transparent, the velocity vectors will be hidden</u> linearly proportional to its value. (color scale is the same as Figure 8.a)) . . . . .	18
12	Bird's eye view of $\sigma_{xz}$ . . . . .	18
13	Evolution of plastic strain and surface topography of the model: M88ConT2 (Table 2). (color scale of topography is the same as Figure 8.a) . . . . .	19
14	The second invariant of strain rates plotted on the reference model's vertical cross-sections along the ridge at 107.5 kyr. Terminations and breakaways are marked by black and red arrows. . . . .	20
15	The weak detachment fault tip reaches the pre-existing shear stress. Plastic strain is plotted with opacity linearly proportional to its value. . . . .	22
16	Velocity of the mass wasting hanging wall. Magnitudes of the velocity are shown by the colors of the arrow heads. Plastic strain is plotted with opacity linearly proportional to its value. . . . .	22
17	Plastic strain, topography and stresses evolution for M28SqrtT1. . . . .	23
18	Along ridge axis $\sigma_{xz}$ (bird's-eye view of three layers of model domain) (positive(red) means clockwise). Plastic strain is plotted with opacity linearly proportional to its value. . . . .	24

19	M28SqrtT1 (Table 2). Bending stress drop (a versus b) at the lower M side due to the cut-back. No bending stress drop (c versus d) at the higher M side as a comparison. . . . .	25
20	New fault front chase after cut-back. . . . .	25
21	Bird's-eye view of the evolution of the hourglass shape median valley. It is generated by attaching the topography of the M28SqrtT1 model to its mirror reflection by assumming symmetrical M variation (0.2 to 0.8 to 0.2). . . . .	26
22	Higher $\sigma_{xx}$ shows inside the median valley on the negative $x$ -axis direction of the ridge axis. . . . .	26
23	Bird's-eye view of the evolution of the corrugations. Color scales for the topography is the same as Figure 8. . . . .	27
24	Evolution of mullion structures. . . . .	28
25	Three functional forms of M variation. M begins to exceed the M = 0.5 black line at Z=10 km, 7 km, 5 km for M28LinT1, M28SinT1 and M28SqrtT1 respectively. . . . .	29
26	Bird's-eye view for comparing the length and timing of inward fault jump. .	30
27	$\partial M / \partial Z$ comparision. . . . .	31
28	Bird's-eye view of the topography. (without vertical exaggeration.) . . . . .	31
29	M57SinT2 versus M57SinT1 (Table 2) . . . . .	33
30	Faulting and stress evolution for M57SinT1. . . . .	34
31	M57SinT2 (Table 2) faulting and stress evolution with respect to time. . . .	35
32	Faulting and stresses evolution (M58SinT1). . . . .	36
33	Plastic strain for M58SinT1 at 350 kyr. . . . .	37
34	Evolution of faulting and morphologies of M58SinT1. . . . .	38
35	Faulting and stresses evolution of M58SinT2. . . . .	39
36	M58SqrtT1 (Table 2) faulting and stress evolution with respect to time. . . .	40
37	Faulting and stresses evolution for M58SqrtT2. . . . .	42

38	M28SinT1 (Table 2) faulting and stress evolution with respect to time. . . . .	43
39	M57LinT1 (Table 2) faulting and stress evolution with respect to time. . . . .	45
40	M57SqrtT2 (Table 2) faulting and stress evolution with respect to time. . . . .	47
41	Trade-off between change in bending force $\Delta F_b$ and weakening in the fault interface $\Delta F_w$ . H is the thickness of the brittle crust and $\gamma$ is the size of initial weak perturbation and A defines the maximum bending force change. (For more details, please refer to [Lavier et al., 2000]) . . . . .	50
42	Comparing nature observation at 13°N Mid-Atlantic Ridge to the Cut back behavior of model M28SqrtT1. The model topography is a mirror symmetric flip according to the dash line, it reveals the case of M varies in a square root functional form from 0.2 to 0.8 to 0.2. For discussion on cut back formation mechanism, please refer to Section ?? . The bathymetry is from GeoMapApp [Ryan et al., 2009]. . . . .	54
43	Comparing nature observation at 13°N Mid-Atlantic Ridge to the Cut back behavior of model M28SqrtT1. The model topography is a mirror symmetric flip according to the dash line, it reveals the case of M varies in a square root functional form from 0.2 to 0.8 to 0.2. For discussion on cut back formation mechanism, please refer to Section ?? . . . . .	55

# 1 Introduction

Around 70% area of the Earth's crust is the oceanic crust. New oceanic crust is constantly forming at the mid-ocean ridges (MORs), the longest mountain chains on the Earth. Seismic and volcanic activities are frequently happening along the MORs due to incessant seafloor spreading and magma upwelling. The interactions between the tectonics and magmatism along the MORs are considered to be responsible for the variations in the seafloor morphology [Buck et al., 2005; Tucholke et al., 2008]. Geodynamic modeling along with a variety of geological, geophysical observation and lab experiment constraints have been used to study how does the interaction system between tectonics and magmatism at the MORs work under geological time scale [e.g. Tucholke and Lin, 1994; Blackman et al., 2002; Behn et al., 2006; Behn and Ito, 2008; Ito and Behn, 2008; Baines et al., 2008; Escartín et al., 2008; Canales et al., 2008; Dick et al., 2008; Dannowski et al., 2010; Olive et al., 2010; Reston and Ranero, 2011; Reston and McDermott, 2011;].

## 1.1 Review of Literature

According to [Fowler, 2004], variations in mid-ocean ridge morphologies are mainly controlled by four factors: magma supply, tectonic strain, hydrothermal circulation and spreading rate.<sup>XT:</sup>Clarify the relationship between the four factors and try to cite the original work for each of them. (in Fowler2004, they didn't mention the ref for these four factors, page417 Chapter9.4.1) Among them, the spreading rate shows the strongest correlation with the ridge morphology. Slow-to-intermediate spreading ridges (half spreading rate less than 4 cm/yr) produce median valleys that are typically 10~20 km wide and 1~2 km deep (e.g., Mid-Atlantic Ridges, Fig. 1a). Fast-spreading ridges (half spreading rate greater than 5 cm/yr) like the East Pacific Rise have axial highs that are 10~20 km wide, 0.3~0.5 km high (Fig. 1b).

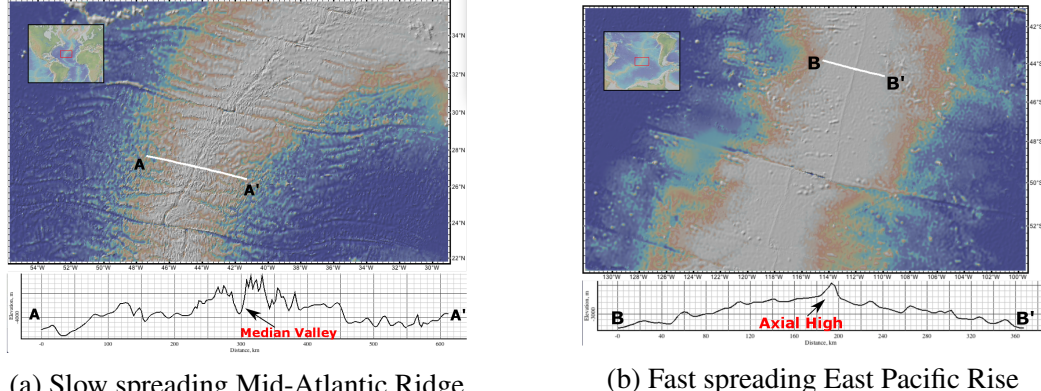


Figure 1: Profiles of bathymetry across MORs.

Slow spreading ridges exhibit along-axis variations in the width and depth of median valleys, crustal thickness and off-axis morphology. Figure 2 shows that the topographic profile near to the center of the ridge segment (A-A') is rather symmetric and has higher frequency. The maximum relief is about 1 km. In contrast, the near-tip profile (B-B') is asymmetric, has much lower frequency, and shows a greater relief ( $\sim 3$  km). The maximum along-axis variation in crustal thickness  $\Delta H_c$  is linearly increasing with segment length L [Chen and Lin, 1999] and the relationship is  $\Delta H_c(L) = 0.0206L$  (Figure 3).

*EC:* [Discussion on off-axis morphology is missing.]

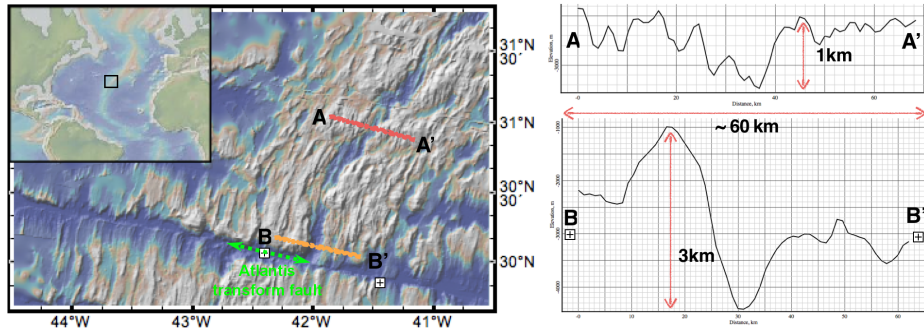


Figure 2: Two bathymetric profiles across the Mid-Atlantic Ridge around  $30^\circ\text{N}$  with vertical exaggeration of 10. A-A' is closer to the segment center while B-B' is at the tip of the segment.

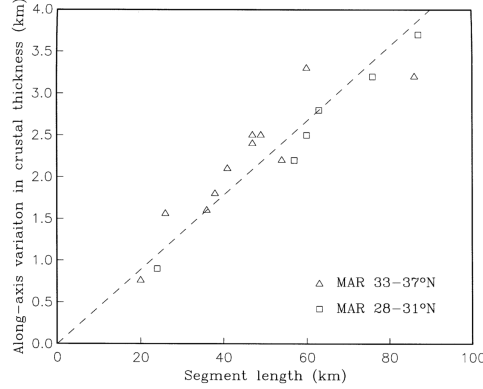


Figure 3: Relationship between the maximum crustal thickness variations ( $\Delta H_c$ ) along a ridge segment and the segment length (L). The dashed line is the best-fit linear regression of the combined data. [Chen and Lin, 1999]

Magma supply at the MORs is mostly a passive process when no hot plume is present [Fowler, 2004]. Driven by both vertical pressure difference and buoyancy due to horizontal density difference, hot mantle rises up to fill the vacated room produced by the plate separation. Since lithostatic pressure decreases with shallower depth in the crust, decompression of the upwelling hot mantle results in partial melting. The generated magma upwells to the upper crust and supplies the diking at the ridge center which releases extensional stresses resulting from the extension forces (e.g slab pull, viscous mantle drag) that drive the seafloor spreading.

The passive nature of the melting processes at the MORs leads to the major difference between fast and slow spreading ridges. At fast spreading ridges, due to much higher spreading rates, vacated room is frequently produced by plates separation. This results in a relatively sufficient magma supply for the frequent diking that can approximately release all the tensional stress generated by plates extension. However, the amount of magma supplied at the slow spreading ridges is restricted by the lower rate for generating vacated room by plates separation. Diking can only partially releases the tensional stress under the limited magma supply and thus the oceanic lithosphere experiences internal deformations (e.g. tectonics process like normal faulting) when the accumulated extensional stress exceeds the strength of the crust.

Buck et al. [2005] attributed the contrasting faulting patterns and ocean floor morphology of fast- and slow-spreading ridges to the difference in the amount of diking-accommodated plate extension. They defined the ratio between the rates of diking and plate separation as  $M = V_{dx}/2V_x$ , where  $V_{dx}$  is the rate of opening by diking at a MOR and  $V_x$  is the half spreading rate of the MOR. According to this definition,  $M = 1$  represents the case where dike injection is so frequent that magma supply is sufficient to release all the tensional stresses from plate separation.  $M = 0$  corresponds to the case of no magma supply, in which diking does not account for any of the plate motion and therefore plates kinematics requires plates to go through internal deformations. As shown in Figure 4, an axial high forms at a fast spreading ridge ( $M = 1$ ) due to buoyancy from lateral density difference across ridge axis but a median valley forms at a slow-spreading ridge ( $M = 0.5$ ) due to near-axis normal faulting, which is in turn caused by the stretching of oceanic lithosphere.

Tucholke et al. [2008] expand the investigation on the role of  $M$  in the mid-ocean ridge mechanics. They focus on the faulting behaviors of slow spreading ridges and find that the OCCs are most likely to form when  $M$  varies from 0.3 to 0.5. When  $M = 0.7$  (Fig. 5), repeated diking pushes faults that have formed at the spreading center away from the ridge axis. Since the thickness of the brittle layer increases away from the ridge axis, frictional and bending energy for maintaining the fault also increases. When the energy needed for maintaining an existing fault exceeds the energy for breaking a new near-axis fault, the old fault is replaced by the new one and most of the extension is accommodated by the new fault. When  $M = 0.3\sim0.5$ , the normal fault remains active for a long time and rotates to a very low angle normal fault (detachment fault), exhuming the lower crust and mantle materials to the seafloor. When  $M < 0.3$ , most of the tension is accommodated by intra-plate deformations rather than by diking and as a result, faulting pattern is more complicated and unsteady.

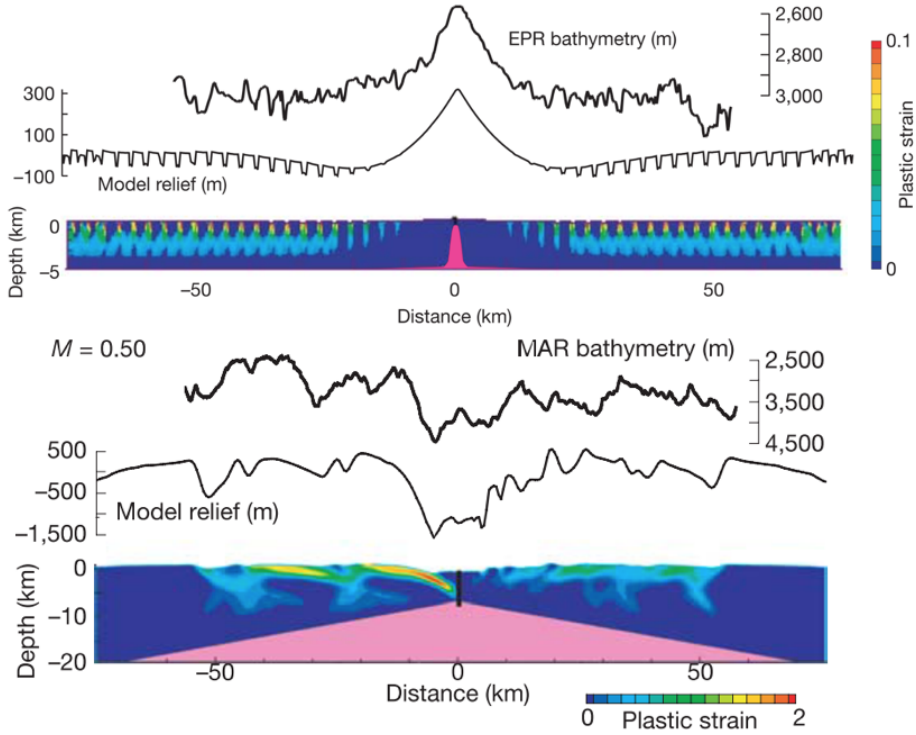


Figure 4: Upper one: modeling result for fast spreading agrees well with the observation of East Pacific Rise. Lower one: modeling result for slow spreading ridges agrees well with the bathymetry of Mid Atlantic Ridge. [Buck et al., 2005]

## 1.2 Statement of Research Purpose

The M-factor formulation used in the previous 2D models [Tucholke et al., 2008, Buck et al., 2005] successfully explained major features found in across-ridge profiles of seafloor bathymetry. However, 2D models have limitations in studying the along-ridge variations in morphology and faulting patterns. Magma supply at fast spreading ridges seems always sufficient for accommodating plate motions with little variation along the ridge axis. The relatively uniform topography along fast spreading ridges is considered to be consistent with the uniform abundance of the magma supply. However, along the slow spreading ridges, bathymetry, gravity anomaly and results from reflection and refraction seismology show strong correlation with variation in crustal thickness [Ryan et al., 2009, Chen and Lin, 1999, Lin et al., 1990, Tolstoy et al., 1993]. Because oceanic crust is mainly formed by upwelled magma at the ridge, variation in the thickness of the crust implies

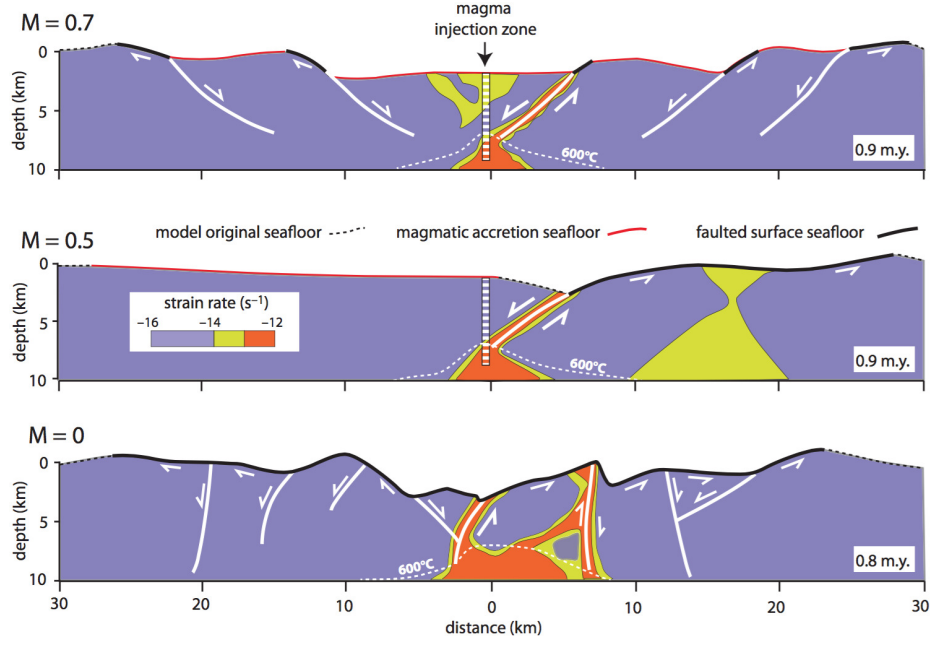


Figure 5: Snapshots of modeled fault behavior and seafloor morphology for values  $M = 0, 0.5$ , and  $0.7$ ; model allows thermal evolution. Structural interpretation is superimposed on modeled distribution of strain rate; model time is indicated in panels at lower right; dashed white line at bottom is  $600\text{ }^{\circ}\text{C}$  isotherm and approximates the brittle-ductile transition; dashed seafloor is original model seafloor, red seafloor is that formed dominantly by magmatic accretion, and solid bold seafloor is fault surface.[[Tucholke et al., 2008](#), [Whitney et al., 2012](#)]

variation in magma supply. At slow spreading ridges, the degree of cooling by hydrothermal circulation, thermal structures and even local spreading rate [[Baines et al., 2008](#)] also varies both along and across the ridge axis and they appear interrelated. Thus, for slow-to-intermediate spreading ridges, the interactions between tectonics and magmatism at MORs are inevitably 3D processes and 3D numerical models are desirable for better understanding factors controlling both across- and along-ridge topography variations.

The purpose of this thesis is to extend the  $M$ -factor formulation originally developed for 2D models to 3D by implementing it into a 3D numerical modeling code SNAC (StGermaiN Analysis of Continua) [[Choi et al., 2008](#)]. By systematically exploring the behaviors of the 3D models and comparing them with observations, we will be able to better understand how the mid-ocean ridge magmatism and tectonic deformations interact.

## 2 Methods

### 2.1 Method of approach

The numerical modeling code, SNAC (StGermaiN Analysis of Continua), is an explicit Lagrangian finite element code that solves the force and energy ~~XT: find out which one is energy balance equation~~ balance equations for elasto-visco-plastic materials. Figure 6 shows major components of SNAC.

For each time step, strain and strain rates are updated based on the initial or previous velocity fields under the constraints from boundary conditions. A constitutive model returns updated stresses corresponding to these deformation measures. Internal forces are then calculated from the updated stresses, which is plugged into the momentum balance equation together with the body force term. Then, the damped ~~XT: better understand the damped force~~ net force divided by inertial mass yields acceleration at a node point, which is time-integrated to velocity and displacement.

A 3D domain is discretized into hexahedral elements, each of which is in turn divided into two sets of tetrahedra. This symmetric discretization prevents faulting from favoring a specific direction or “mesh grains”.

Rheology for the oceanic lithosphere is assumed to be elasto-visco-plastic (EVP). When viscosity is high at low temperature, the EVP rheology implemented in SNAC essentially becomes the Mohr-Coulomb plasticity with strain softening that can create shear bands that behave like faults. Strain softening is realized by cohesion decreasing with increasing amount of permanent (i.e., plastic) strain. I assume this relationship is linear for simplicity. It is sufficient for a full description of such a linear strain weakening to define initial and final values of cohesion and a critical plastic strain at which cohesion becomes the final value. I define the rate of strain weakening as the cohesion difference divided by the critical plastic strain and use it as one of the model parameters. When temperature is high and viscosity is low, the rheology becomes the Maxwell viscoelasticity and can

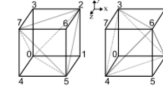
model creeping flow. This property of the EVP model makes it possible to set up a structure with a brittle lithosphere and a ductile asthenosphere through a proper temperature distribution. Rheological parameters are taken from previous studies that use a similar rheology [e.g., [Buck et al., 2005](#); [Tucholke et al., 2008](#)] or from lab experiments [e.g., [Kirby and Kronenberg, 1987](#)].

For 3D dikeing processs, the strain  $\Delta\varepsilon_{xx}$  associated with dikeing leads to stresses changes,  $\Delta\sigma_{xx}$ ,  $\Delta\sigma_{yy}$  and  $\Delta\sigma_{zz}$ . These stress changes due to dikeing are computed according to the linear elastic constitutive equations  $\sigma_{ij} = \lambda\varepsilon_{kk}\delta_{ij} + 2\mu\varepsilon_{ij}$ .

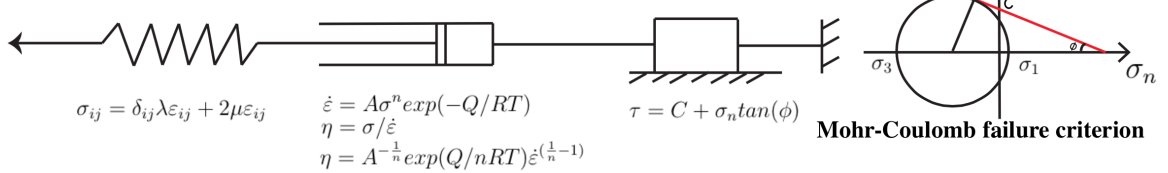
**SNAC:** a 3D, MPI parallelized, updated Lagrangian explicit finite difference code for modeling long-term tectonic evolution of the Earth's elasto-visco-plastic crust and mantle. (Choi et al., 2008)

$$\text{Momentum Balance Equation: } \frac{\partial\sigma_{ij}}{\partial x_j} + \rho g_i = \rho \frac{Dv_i}{Dt}$$

**Spatial Decritization:** A 3D domain is discretized into hexahedral elements, each of which is filled with two sets of 5 tetrahedra.



**Elasto-Visco-Plastic (EVP) Rheology:**



**Diking M Formulation:**  $M = Vdx / 2Vx$  ( $Vdx$  is the dike accretion strain(dike widening) $\Delta\varepsilon_{xx}$  in each time step dt)

Stresses introduced by a dike accretion strain(dike widening) $\Delta\varepsilon_{xx}$  in each time step dt:

$$\Delta\sigma_{xx} = (\lambda + 2\mu)\Delta\varepsilon_{xx} \quad \Delta\sigma_{yy} = \lambda\Delta\varepsilon_{xx} \quad \Delta\sigma_{zz} = \lambda\Delta\varepsilon_{xx}$$

**Mohr-Coulomb failure criterion**

Figure 6: Essential components of the numerical method.

## 2.2 Model Setup

The 3D models have a common geometry of  $60 \text{ km} \times 20 \text{ km} \times 20 \text{ km}$  in  $x$ ,  $y$  and  $z$  axes

*EC:* [Correct the orientation of the coordinate axes. Y is vertically upward] respectively

with a resolution ( $\Delta x$ ) of 1 km (i.e.,  $\Delta x$  is the size of each hexahedron element). The initial temperature field linearly increases from  $0^\circ\text{C}$  at the top surface to  $240^\circ\text{C}$  at the depth of 6 km, reflecting enhanced cooling due to hydrothermal circulation (Fig. 7). Below 6 km, the temperature profile follows the semi-infinite half-space cooling model of moving

plates [e.g., [Turcotte and Schubert, 2002](#)]. Two sides perpendicular to the  $z$  coordinate axis are free-slip. The top surface has vertical tractions from water columns, of which heights are locally determined as  $(4000 - h(x, z))$  m, where  $h(x, z)$  is the topography at a location,  $(x, z)$ . The bottom surface is supported by the Winkler foundation. Temperature is fixed at 0 °C on the top surface and at 1300 °C on the bottom surface.

Diking, represented by the factor  $M$  as described above, is assumed to occur in the middle of the domain (Fig. 7), where lithosphere is thinnest.

We adopt the linear isotropic elasticity, power-law viscosity of dry diabase [e.g., [Kirby and Kronenberg, 1987](#), [Buck et al., 2005](#)] and the Mohr-Coulomb plastic model. The complete list of model parameters are given in Table 1.

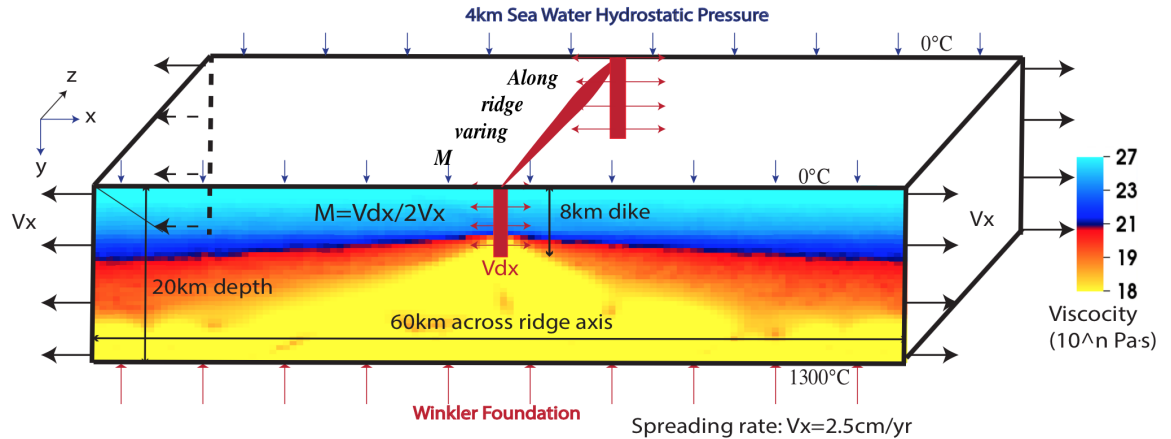


Figure 7: Model setup

## 2.3 Parameters to control

Before running 3D models, I have run hundreds of pseudo-2D models for initial setup and benchmarking with previous studies [e.g., [Buck et al., 2005](#), [Tucholke et al., 2008](#)]. Preliminary pseudo-2D results show that the model behavior in faulting pattern is sensitive to the rate of strain weakening. Two cases of strain weakening are tested in the 3D models. In one case (denoted as Type 1 weakening), cohesion linearly decreases from 44 MPa (denoted as  $C_i$ ) to 4 MPa ( $C_e$ ) for plastic strain accumulating from 0 ( $\varepsilon_p^1$ ) to 0.1

$(\varepsilon_{pe}^1)$ . It has a characteristic fault slip of 150 m for pseudo-2D models and 300 m for 3D models. The other case (Type 2 weakening) assumes cohesion linearly decreasing from 44 MPa ( $C_i$ ) to 4 MPa ( $C_e$ ) for plastic strain accumulating from 0 ( $\varepsilon_{pi}^2$ ) to 0.33 ( $\varepsilon_{pe}^2$ ). In this case, the characteristic fault slip for pseudo-2D models is 500 m and for 3D models is 1 km. The characteristic fault slip is defined as  $\Delta X_c = 3 \Delta x \varepsilon_{pe}$  where  $3 \Delta x$  represents the thickness of the shear bands which is usually 2 to 4 times  $\Delta x$  (size of a hexahedron element) [Lavier et al., 2000]. When  $\Delta X_c$  amount of slip takes place at the fault interface, the cohesion of the material at the faulting interface decreases to  $C_e$ . In this way, under the same amount of  $\Delta X_c$ , models with different resolution should produce the same faulting patterns.

Meanwhile, although how to estimate the M values from observations is a subject of on-going research, we do have constraints from a large dataset of bathymetry, gravity and seismic surveys as well as geological drilling. Generally, at slow spreading ridges, magma supplies mostly at the center of the ridge segment and decreases towards the tip of the segment [Tolstoy et al., 1993, Chen and Lin, 1999, Carbotte et al., 2015]. There is also evidence for shorter wavelength of 10 to 20 km discrete focus of magma accretion along the ridge axis [Lin et al., 1990]. Based on these constraints, I start considering a few scenarios of variations in M along the ridge axis. They are three M ranges (i.e. 0.2~0.8 (M28), 0.5~0.7 (M57) and 0.5~0.8 (M58)) with three simple functional forms of M variations (i.e. linear, sinusoidal and square root).

The numerical cost of a 3D model is non-trivial. For 2 Myr of model time, each model usually runs on 192 cores for about 48 hours (i.e., around  $10^4$  core-hours). Under this constraint of computational cost, I control only the following three parameters while fixing all the others: 1) three types of functional forms (i.e. linear, sinusoidal and square root); 2) three ranges of M variation along the ridge axis (0.5~0.7 (M57); 0.5~0.8 (M58); 0.2~0.8 (M28)) and 3) two types of weakening rate (Type 1 and Type 2).

Till now,  $11 + 1$  3D models are run (11 models with M varying along the ridge-axis

and 1 model with constant  $M = 0.8$ . The complete list of 3D models is given in Table 2.

Table 1: Summary of 3D Model Parameters

Number	Variable	Description	Value	Units
1	$W_{dike}$	Dike width	2	km
2	$D_{dike}$	Dike depth	8	km
3	$H$	Crustal thickness at dike	6	km
4	$dT/dy$	Crustal thermal gradient	40	K/km
5	$T_1$	Temperature at lower boundary of crust	240	°C
6	$g$	Gravity acceleration	10	m/s <sup>2</sup>
7	$demf$	Dimensionless force damping factor	0.8	N/A
8	$dt$	Time step	1.5768e+07	second
9	$topokappa$	Parameter for topography smoothing	0	N/A
10	$shadowDepth$	Ghost elements for parallel computing	2	N/A
11	$meshI$	Mesh number in X direction	60	N/A
12	$meshJ$	Mesh number in Y direction	20	N/A
13	$meshK$	Mesh number in Z direction	20	N/A
14	$L_I$	Length in X direction	20	km
15	$L_J$	Length in Y direction	20	km
16	$L_K$	Length in Z direction	20	km
17	$\rho$	Density	3000	kg/m <sup>3</sup>
18	$\lambda$	Lamé's constant	30	Gpa
19	$\mu$	Shear modulus	30	Gpa
20	$refvisc$	Reference viscosity	0.125e-17	Pa <sup>-n</sup> /s
21	$activationE$	Activation Energy	276.0e+3	kJ/mol
22	$vis_{min}$	viscosity minimum cutoff	1.0e+18	Pa * s
23	$vis_{max}$	viscosity maximum cutoff	1.0e+27	Pa * s
24	$srexponent$	Power of power law in viscosity	3.05	N/A
25	$\varepsilon_{p_i}^1$	initial plastic strain for piecewise Type 1 weakening	0	N/A
26	$\varepsilon_{p_i}^2$	initial plastic strain for piecewise Type 2 weakening	0	N/A
27	$\varepsilon_{p_e}^1$	end plastic strain for piecewise Type 1 weakening	0.1	N/A
28	$\varepsilon_{p_e}^2$	end plastic strain for piecewise Type 2 weakening	0.33	N/A
29	$C_i$	initial Cohesion for piecewise weakening	44	Mpa
30	$C_e$	end Cohesion for piecewise weakening	4	Mpa
31	$\phi$	Friction angle	30	°
32	$remesh_{timestep}$	Remesh when timestep reach its value	400000	N/A
33	$remesh_{length}$	Remesh when the global minimum of the ratio of the volume of a tetrahedron to one of its surface area	0.6	N/A
34	$topTemp$	Surface temperature	0	°C
35	$bottomTemp$	Bottom temperature	1300	°C
36	$V_x$	Half spreading rate	7.9e-10	m/s

Table 2: List of 3D numerical experiments.

Model	M range	Functional Form	Type of weakening	For short
1	M28	Linear	Type 1	M28LinT1
2	M28	Sinusoidal	Type 1	M28SinT1
3	M28	Square Root	Type 1	M28SqrtT1
4	M57	Linear	Type 1	M57LinT1
5	M57	Sinusoidal	Type 1	M57SinT1
6	M57	Sinusoidal	Type 2	M57SinT2
7	M57	Square Root	Type 2	M57SqrtT2
8	M58	Sinusoidal	Type 1	M58SinT1
9	M58	Sinusoidal	Type 2	M58SinT2
10	M58	Square Root	Type 1	M58SqrtT1
11	M58	Square Root	Type 2	M58SqrtT2
12	M88	Constant	Type 2	M88ConT2

### 3 Results

In this “Results” chapter, I first walk through the reference model (M28LinT1) and compare it with a constant M model (M88ConT2). Then, I describe in detail the major characteristics of the models. Finally, I describe the effects of different weakening rates, ranges of M variation and functional forms of M variation on the main characteristics.

#### 3.1 Reference model M28LinT1

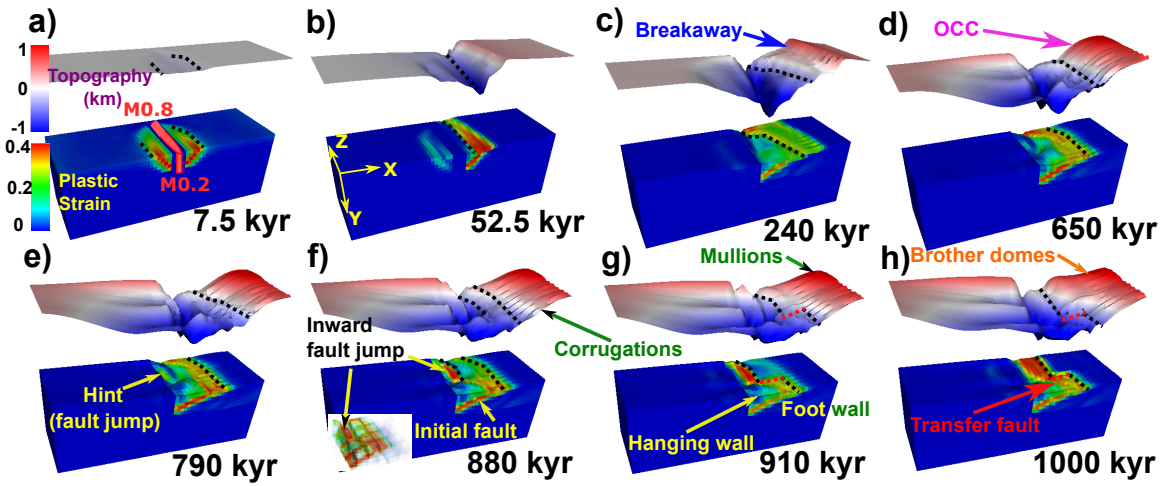


Figure 8: Evolution of plastic strain and surface topography of the reference model M28LinT1 (Table 2). Each snapshot shows plastic strain plotted on the model domain and the five times exaggerated topography. Initial seafloor is marked as a reference of 0 km of the topography. The bold dash lines (black) are the terminations of the detachment faults. The bold dash lines (red) in g and h are the transfer faults that connect the terminations along the ridge. The inset in f plots plastic strain with opacity linearly proportional to its value.

I consider the model with M varies linearly from 0.2 to 0.8 along the ridge axis with type 1 weakening rate (M28LinT1) as the reference model. The major structural features of the model are indicated in the Figure 8. They are breakaway (Figure 8.c); oceanic core complex (OCC) (Figure 8.d); terminations of the detachment faults where the active faulting interfaces reach the seafloor (black dash line); new high angle normal faults forming near the ridge axis, which is termed as “inward fault jump” (Figure 8.f); corrugations

(Figure 8.f) and mullion structures (Figure 8.g); and the side-by-side “brother domes” (Figure 8.h).

The model produces a median valley that widens and deepens with increasing plate extension (Fig. 8a-c). The rate of its widening and deepening at a specific location along the ridge is inversely proportional to the M value (i.e. rate of local magma supply).

For the first 7.5 kyr (Figure 8.a), normal faults, represented by localized plastic strain, begin to form near the ridge axis. Because stresses due to plate motions accumulate faster at the lower M side than at the higher M side, faults first initiate at the lower M side and then propagate to the higher M side. The asynchronous initiation of faults along the ridge axis creates offset in breakaway: i.e., the breakaway at the lower M side extends further than that of the higher M side (Figure 9).

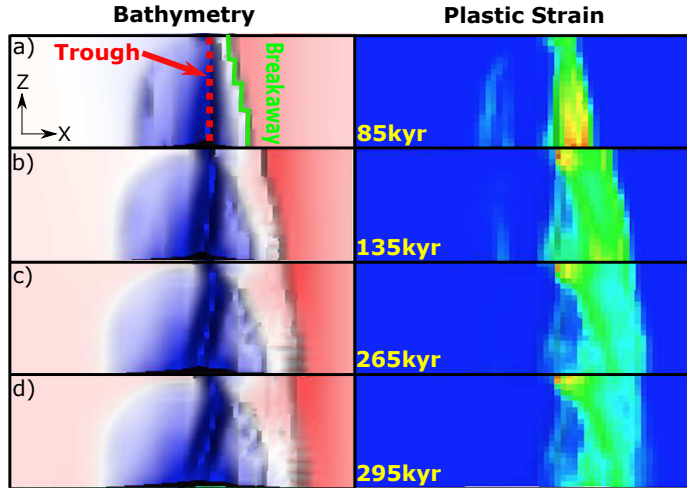


Figure 9: Bird’s-eye view of the evolution of breakaway (marked by green bold line) and depressed narrow zone (“axial trough”) along the ridge axis (red dash line in (a)) for model M28LinT1 (Table 2). This figure share the same color scales with Figure 8.

By 52.5 kyr (Figure 8.b), the normal fault on the right hand side of the ridge axis remains active while the one on the left becomes inactive. As the fault evolves, the upper part of the permanent deformed interface (shown as plastic strain in the model) of the fault is exhumed to the seafloor with its front edge extending away from the ridge axis following the spreading plate. Initially, the extending edge of this fault interface corre-

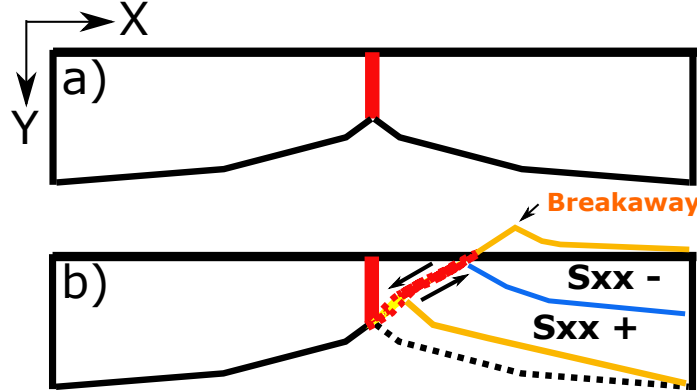


Figure 10: Bending stress illustration. The blue line is the neutral plane where  $\sigma_{xx} = 0$ . Above the neutral plane is compression ( $\sigma_{xx} < 0$ ) and beneath it is tension ( $\sigma_{xx} > 0$ ).

sponds to the right boundary of the plastic strain along the ridge. Note that the extending boundary (tips) of the plastic strain also aligns with the breakaway along the ridge before 265 kyr (Figure 9.a~c).<sup>XT</sup> The previous sentence is for explaining the extending tips of plastic strain The along-ridge offset in  $x$ -direction of the tips of the extending plastic strain reduces at  $\sim 295$  kyr (Figure 9.d) because when the normal fault lasts long enough and bends to a low angle detachment fault at the lower M side, the termination of the detachment fault stops extending and the healing of plastic strain (following Tucholke et al., 2008) implemented in the model reduces quickly the plastic strain of the inactive fault interface that has been exhumed to the seafloor. While at the higher M side, the termination keeps extending and reduces the initial offset generated by the asynchronous initiation of faulting. In addition, as the fault slips, crust at the footwall bends in a clockwise rotation as illustrated by Figure 10.

The active, near-axis normal fault rotates to a lower dip of  $\sim 30^\circ$  at the root of the fault and to  $\sim 0^\circ$  at the exposed fault interface (Fig. 8.c). However, the normal fault at the higher M side (especially for  $M > 0.7$ ) experiences less bending and the termination of the fault is closer to the ridge axis. The maximum relief between the breakaway and the axial trough inside the median valley becomes larger than 1 km. In addition,  $\sim 1$  km wavelength corrugations begin to show up between the breakaway and termination on the lower M side ( $M < 0.3$ ). The corrugations show a uniform wavelength, which is

also smaller than that of the mullion structures (Figure 8.g). Formation mechanism for these structures are discussed in one of the following sections. The axial trough is initially straight and parallel to the ridge axis (Figure 9.a) but becomes oblique to the ridge axis. The obliquity increases with the amount of extension (Figure 9.b,c,d).

By 650 kyr (Figure 8.d), the median valley becomes wider and deeper. The detachment fault reaches its lowest dip angle and its termination stops moving away from the ridge axis. The breakaway of this detachment has already moved out of the model domain. The total fault offset at this point is greater than the thickness of the crust and thus sufficient for exhuming the upper mantle materials. A hint of the inward fault jump appears up over the area corresponding to  $0.5 < M < 0.65$ .

By 790 kyr, a new near-axis fault appears and propagates toward the high M ( $> 0.5$ ) side (Fig. 8.e). However, the initial detachment fault is still active and takes up most of the extension. The distance between the termination of the detachment fault and the ridge axis is greater at the lower M side. Subsequently, the detachment fault becomes less active and the new near-axis fault accommodates most of the intra-plate extension. This event is called the “inward fault jump” [Tucholke et al., 1998; Dick et al., 2008]. The new high angle normal fault cuts through the hanging wall of the detachment fault (Fig. 8.f).

By 910 kyr (Fig. 8.g), the inward fault jump completes in the  $M > 0.5$  region: the new high-angle fault takes up all the extension and the initial detachment fault becomes completely inactive. The block that was previously a hanging wall to the detachment becomes footwall of the new fault and moves with the spreading plate to the positive  $x$ -axis direction. At the lower M side, the detachment is still active and the hanging wall continues to move toward the negative  $x$ -axis direction (Figure 11). This opposite sense of relative motions between the high and the low M side creates a region of EC: dextral [Isn't it sinistral?] shear and eventually creates a transfer fault (Fig. 8.h).

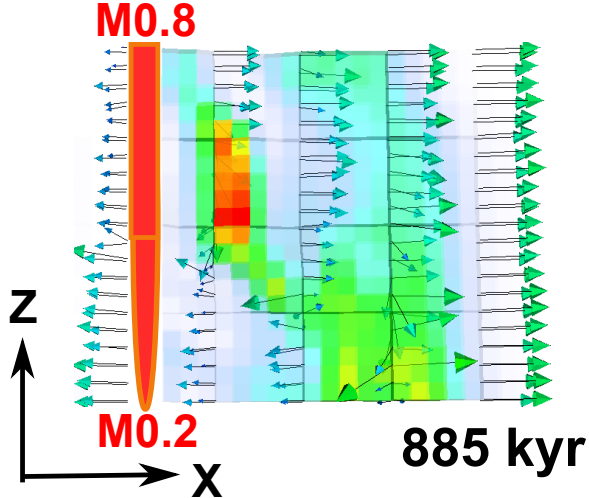


Figure 11: Bird's-eye view of velocity field with plastic strain plotted with [EC: opacity \[why do you need transparency in this figure?\]](#) [XT: if not transparent, the velocity vectors will be hidden](#) linearly proportional to its value. (color scale is the same as Figure 8.a))

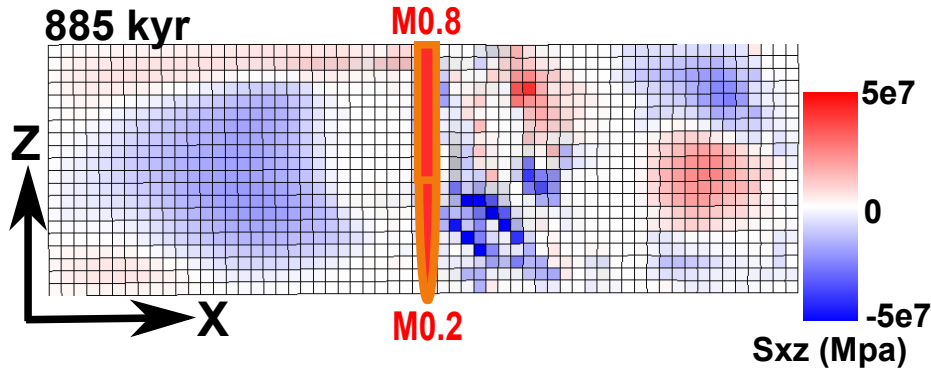


Figure 12: Bird's eye view of  $\sigma_{xz}$ .

### 3.1.1 Constant M model M88ConT2

As a comparison to the varying M models, a constant M model is run.

As shown in Figure 13, model M88ConT2 produces a  $\sim 20$  km wide and  $1 \sim 2$  km deep median valley, which is similar to the generally observation of the Mid-Atlantic Ridges. The width and depth of the median valley is almost constant along the ridge as contrast to the varying M models. The variation of the location of the breakaway and termination along the ridge that is mentioned in the reference model (M28LinT1) does not show up. Because the magma supply is constant along the ridge with  $M = 0.8$ , there is no stress perturbation along the ridge. Thus, the normal faults along the ridge initiate at the

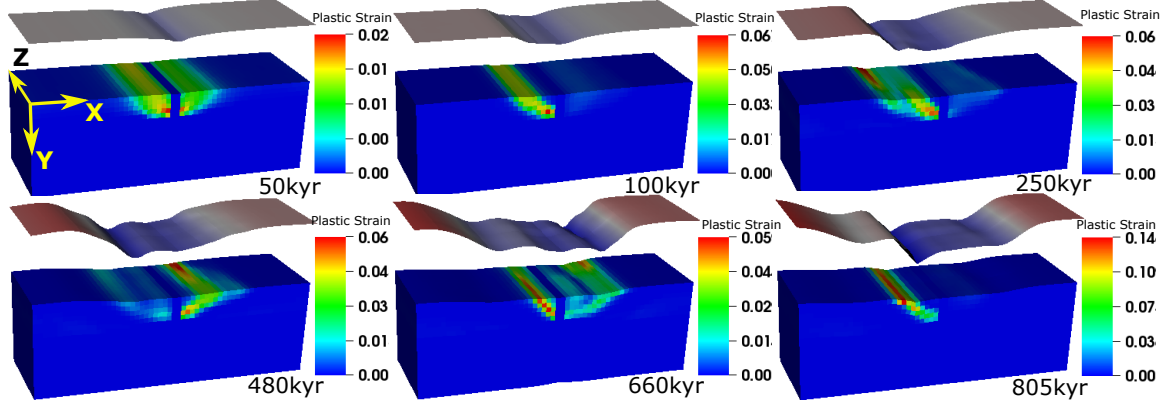


Figure 13: Evolution of plastic strain and surface topography of the model: M88ConT2 (Table 2). (color scale of topography is the same as Figure 8.a)

same time and the slipping rate of the fault is also constant along the ridge axis. The synchronized fault initiation results in no offset between breakaways and the constant slipping rate produces no along ridge axis variation in the position of the termination. In addition, neither corrugations nor mullion structures are generated. Normal faults alternate on each side of the ridge axis with a period of  $\sim 300$  kyr due to the mechanism mentioned in the “Introduction” section for the 2D models of  $M > 0.5$ . This fault alternation produces symmetrical high frequency abyssal hills. For 3D models, why and how fault alternates on each side of the ridge axis is different from the previous 2D studies and is described in the following sections.

### 3.2 Main characteristics of the models

I identify seven features that are common to most of the models: location of the termination, geometry of the trough, inward fault jump, fault alternation, mass wasting, hourglass-shaped median valley and corrugations and mullion structures. Since the details of these features differ among the models, they are useful for delineating and contrasting complicated model behaviors.

### 3.2.1 Location of *EC*:termination [I think “fault trace” is what you mean.]

*XT*:for the term “termination” please refer to: 23 times usage from [Canales et al., 2008] or [Blackman et al., 2009] or figure one of [Dick et al., 2008] or figure six of [Mallows and Searle, 2012] or figure 1,2,3A of [Schouten et al., 2010] But [Reston and Ranero, 2011] give a further discussion on it and they favor “top hanging wall cutoff”. they also mention that “The traditional map term fault trace, which is not generally used on sections, is not appropriate as it cannot be used to describe the geometry of a structure everywhere buried by later sedimentary rock.”

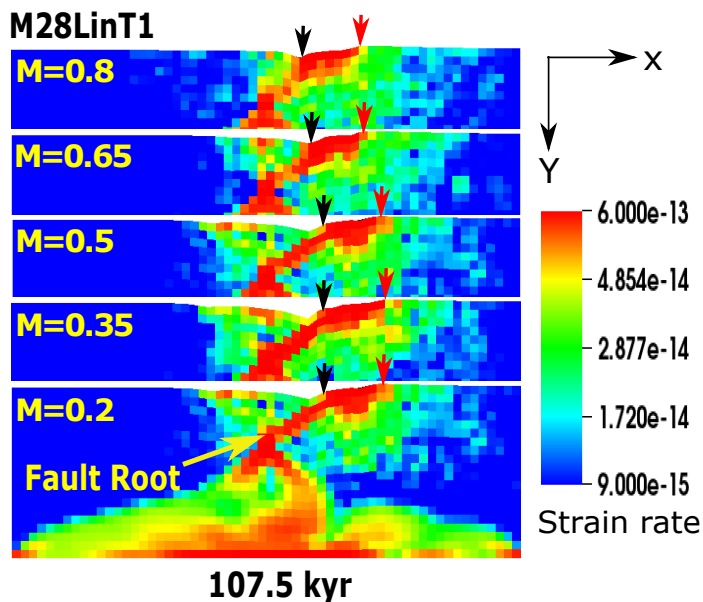


Figure 14: The second invariant of strain rates plotted on the reference model’s vertical cross-sections along the ridge at 107.5 kyr. Terminations and breakaways are marked by black and red arrows.

The location of a fault trace is delineated by black dashed lines in Figure 8 and marked by black arrows in Figure 14. The reference model shows that distance from the ridge axis to *fault trace* the termination of the detachment fault is greater on the lower M side than on the higher M side because faulting starts on the lower M side first and initiates later on the higher *XT*: I have been using higher M side and lower M side instead of high or low M side M side.

### 3.2.2 Geometry of axial trough

The depressed narrow region inside the median valley is termed as “trough”<sup>EC:</sup> [In my opinion, “axial trough” would be better].<sup>XT:</sup> However, axial trough is usually used for fast spreading and axial sounds like on the central axis of the ridge, However, this trough describing here is for the lowest points insdie the median valley of slow spreading ridge that can become a curve and be off the axis The reference model showed that its shape in the map view evolves from a straight line parallel to the ridge axis to a line oblique to the ridge-axis (Figure 9). Initially, the trough corresponds to the fault trace. As the normal fault rotates to a lower dip on the lower M side, the trough is no longer coincident with the fault trace. The axial trough on the higher M side ( $M > 0.5$ ) are pushed away from the ridge axis [Tucholke et al., 2008]. However, since <sup>EC:</sup> the trough cannot bypass the termination [What do you mean?] the trough is to the side which is nearer to the ridge axis than termination, it cannot bypass termination further away from the ridge axis, the trough at  $M = 0.8$  is restricted at the termination. Together it generates the curved trough (Figure 9).

### 3.2.3 Inward fault jump

The inward fault jump occurs in all the models when an old fault locks and a new one forms near the ridge axis (e.g., Fig. 8).<sup>XT:</sup> for the description of the previous commented out paragraph, please refer to: [Lavier et al., 2000; Olive et al., 2014]

The new fault usually forms on the high M side first and it connects to the existing detachment developing on the lower M side ( $M < 0.5$ ), creating a curved fault trace. Unlike fault alternation, the inward fault jump occurs on the same side of the ridge axis and its along-axis extent corresponds to the  $M > 0.5$  region.

### 3.2.4 Fault alternation

When  $M$  is high enough, a normal fault first forms on one side of the ridge axis but another fault forms on the other side when the first one locks (Fig. 13) [Buck et al., 2005,

Tucholke et al., 2008]. This behavior is termed as “fault alternation”.

### 3.2.5 Cut-back

*XT:* How about change Cut-back to shear-wasting or mass wasting or cut-wasting *EC:* [Mass wasting sounds most appropriate.]

*XT:* For “shear-wasting”, shear is from the three triggering shear stresses, wasting is from mass wasting. For mass wasting, it has the benefit that people are familiar with this term, however, the new mechanism for triggering it(the shear stress) is missing *EC:* [Didn’t we agree that shear stress seen in the vertical cross-section does not trigger this event?]

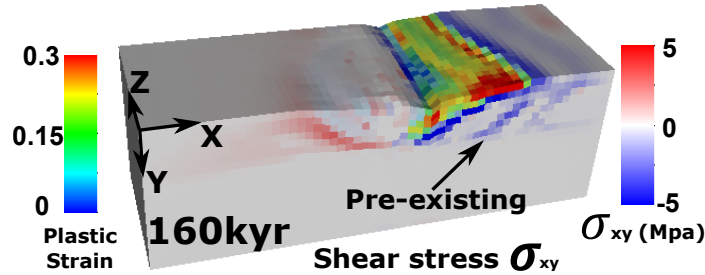


Figure 15: The weak detachment fault tip reaches the pre-existing shear stress. Plastic strain is plotted with opacity linearly proportional to its value.

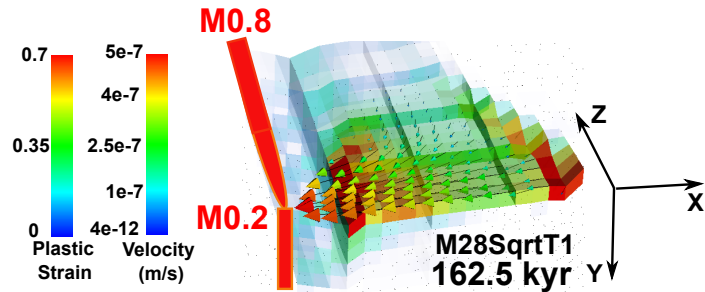


Figure 16: Velocity of the mass wasting hanging wall. Magnitudes of the velocity are shown by the colors of the arrow heads. Plastic strain is plotted with opacity linearly proportional to its value.

Mass wasting occurs on the exposed surface of a low-angle normal fault. When a layer of weak fault interface becomes gravitationally unstable and is detached from the underlying material, the detached layer flows towards the ridge axis and the lower M side

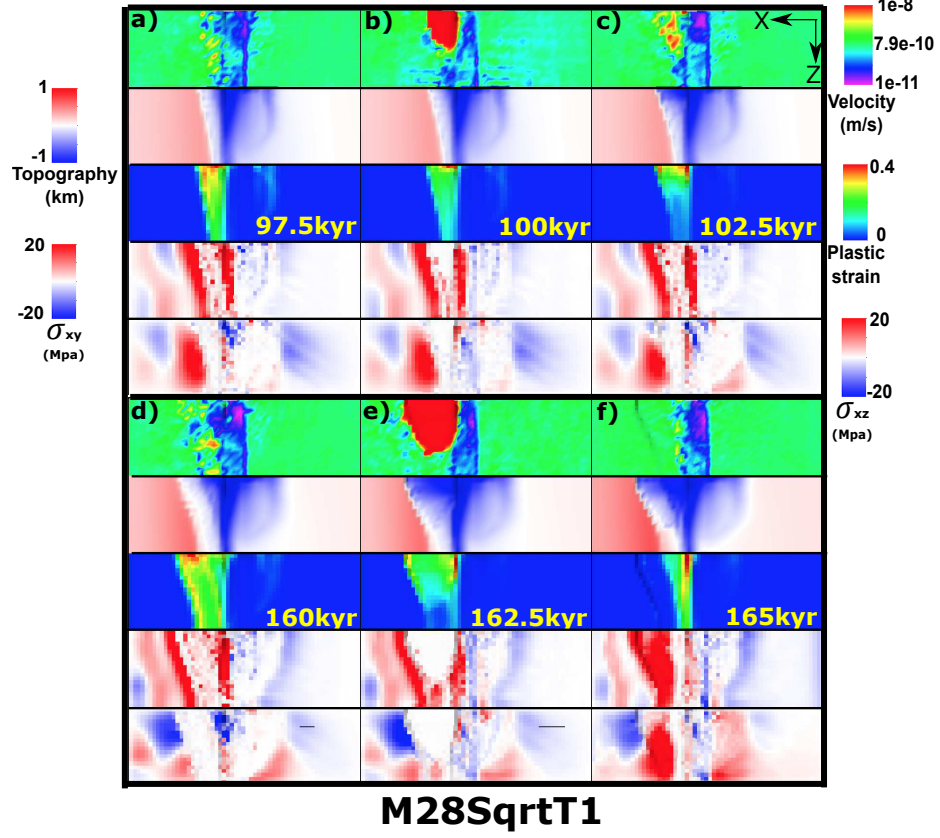


Figure 17: Plastic strain, topography and stresses evolution for M28SqrtT1.

with a velocity  $\sim 10$  times faster than the half spreading rate (Figure 16; Figure 17.b,e (first row))). The mass wasting produces a continuous fault scarp with a relief of  $\sim 1$  km along the initial breakaway.

Immediately after an event of mass wasting, the fault trace jumps towards the ridge axis (Figure 17.d versus f (third row: plastic strain)). Then,  $\sigma_{xy}$  and  $\sigma_{xz}$  soon <sup>EC:</sup> fill in the area [What do you mean by “stresses filling an area”?] between cut-back created fault scarp and the new termination (Figure 17.f (fourth and fifth row:  $\sigma_{xy}$  and  $\sigma_{xz}$ ). <sup>EC:</sup> [don’t understand the rest of this paragraph.] After that, the termination at the higher M side extends faster and further than the lower M side (Figure 20.a~d). This is because during the cut-back, tensional stress due to bending is released at the lower M side but continues to accumulate at the higher M side. At the lower M side, it needs time to reach the previous tensional stress state and then starts from there to pull the new termination away from

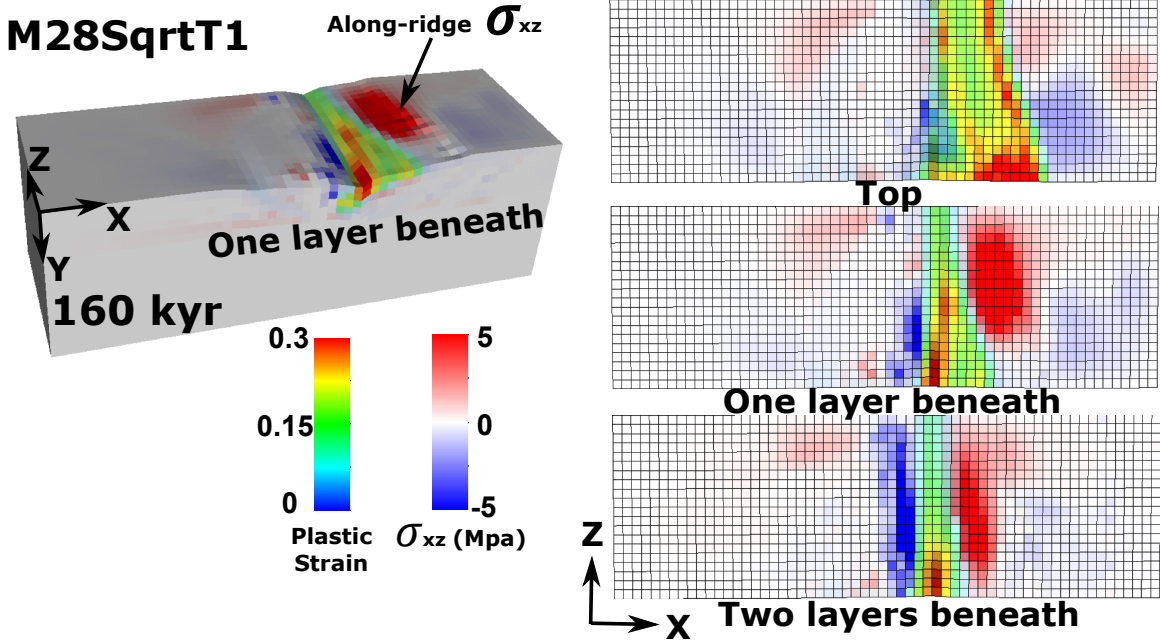


Figure 18: Along ridge axis  $\sigma_{xz}$  (bird's-eye view of three layers of model domain) (positive(red) means clockwise). Plastic strain is plotted with opacity linearly proportional to its value.

the ridge axis. While at the higher M side the increasing tensional stress directly leads to a fast extending termination.

This phenomenon is responsible for the corrugations observed. It creates an “X” shape “scan” that first “scan” the topography with the faster low M side (Figure 17.d and e) and then “scan” with the faster higher M side (Figure 20.c and d). This results in a evolving curved termination that produces mullion structures (Figure 20.d). *EC: [Can't follow what you say.]*

### 3.2.6 Hourglass-shaped median valley

A median valley takes a hourglass shape whenever M varies along the ridge. The hourglass shapes vary with time and the functional form of M variation. A median valley initially has similar width along the ridge but is deeper on the lower M side where normal faults first form. By  $\sim 100$  kyr (Figure 21.b), the fault on the negative  $x$ -axis direction of the ridge axis doesn't propagate to the higher M side of the ridge and becomes inactive.

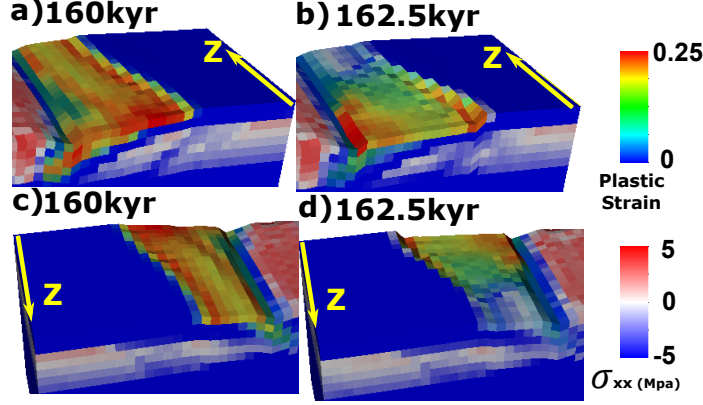


Figure 19: M28SqrtT1 (Table 2). Bending stress drop (a versus b) at the lower M side due to the cut-back. No bending stress drop (c versus d) at the higher M side as a comparison.

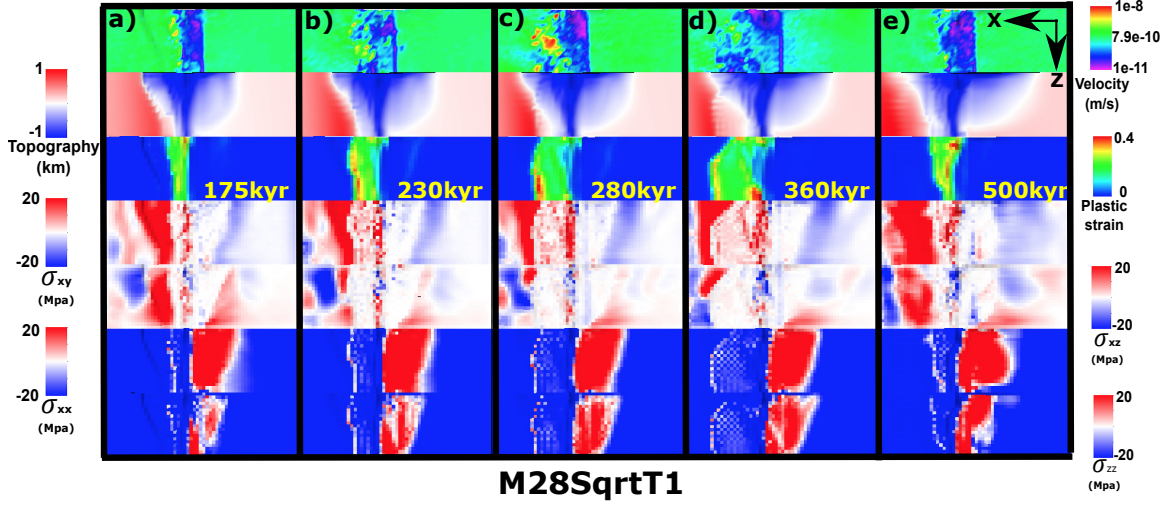


Figure 20: New fault front chase after cut-back.

It produces a depressed topography curve following the inactive fault trace, which is further away from the ridge axis at the lower M side but closer to ridge axis at the higher M side. On the other side of the ridge axis, as the active fault rotates to a lower dip angle, it generates breakaways that are further away from the ridge axis at the lower M side while closer to the ridge axis at the higher M side. This along ridge variation in the location of the breakaways act as another boundary of the hourglass. Both boundaries are extended following the spreading plates. By  $\sim 170$  kyr (Figure 21.c), the hourglass become wider and deeper. Since the area of the cross-section along the ridge inside the hourglass shape median valley is approximately inversely proportional to the local M values, the shape of

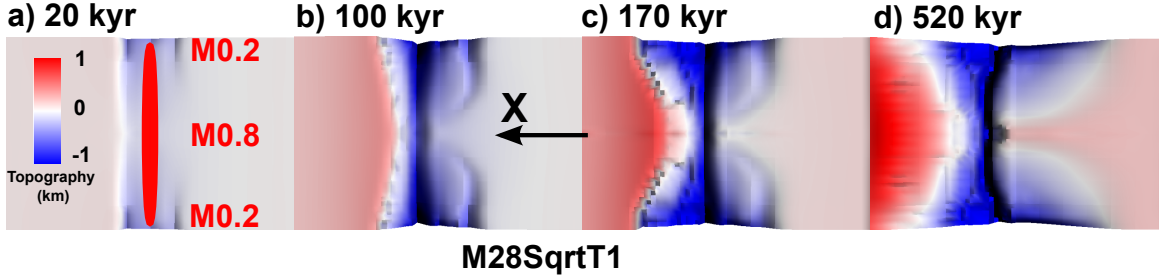


Figure 21: Bird's-eye view of the evolution of the hourglass shape median valley. It is generated by attaching the topography of the M28SqrtT1 model to its mirror reflection by assuming symmetrical M variation (0.2 to 0.8 to 0.2).

the hourglass varies with different M variations.

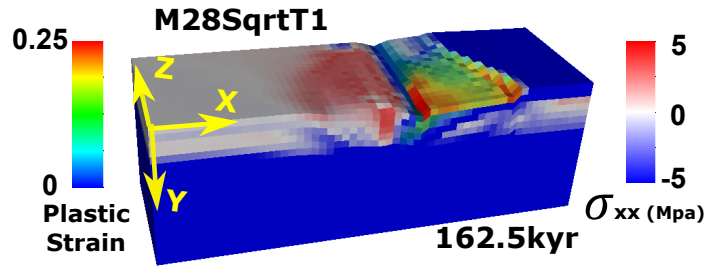


Figure 22: Higher  $\sigma_{xx}$  shows inside the median valley on the negative  $x$ -axis direction of the ridge axis.

The further depression inside the median valley is mostly due to the elastic deformation from crustal extension. As shown in Figure 22, the  $\sigma_{xx}$  in the median valley is higher because that the brittle crust is the thinnest at the median valley, when same amount of force propagates from far field extension to the median valley, the stress increases. This increased  $\sigma_{xx}$  is responsible for the further depression and extension of the median valley on the negative  $x$ -axis direction of the ridge axis (Figure 21.d). For the median valley on the other side of the ridge axis, cut-back triggered mass wasting between the breakaways and the ridge axis results in the further lowering in topography (Figure 17.d versus e (topography)).

### 3.2.7 Corrugations and mullion structures

Both corrugations and mullion structures are linear structures parallel to the spreading direction. As shown in Figure 8.f, at the  $M < 0.5$  area on top of the OCC surface, corrugations show a uniform wavelength of  $\sim 1$  km with hundreds meters in amplitude. While at the higher  $M$  side of the ridge (Figure 8.g), a mullion structure of a wavelength of  $\sim 7$  km. In spite of morphological similarity, corrugations and mullion structures have different formation mechanisms.

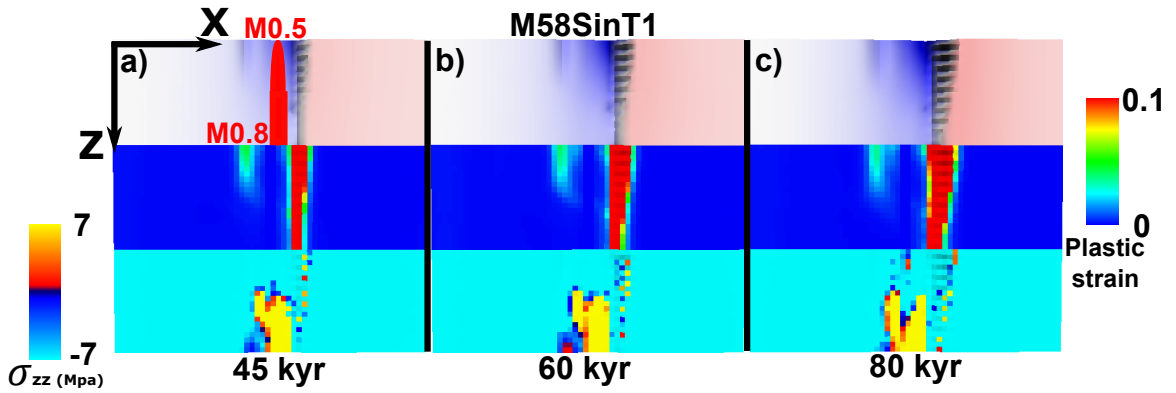


Figure 23: Bird's-eye view of the evolution of the corrugations. Color scales for the topography is the same as Figure 8.

### Corrugations

**Corrugations** The corrugation is produced at the front tip of the [EC: extending](#) [What do you mean by “extending” plastic strain?] plastic strain by tensile failure in the along- $z$ -axis direction. As shown in Figure 23, when the plastic strain reaches or exceeds 0.1 (red color), base on type 1 weakening, the cohesion decreases to 4 Mpa. With a  $30^\circ$  friction angle, tensile failure is declared when the  $\sigma_{zz}$  reaches  $\sim 7$  Mpa (yellow color). The tensile stress is due to the asynchronous faulting along the ridge. Faulting initiates earlier at the lower  $M$  side of the ridge. As the fault offsets more on the low  $M$  side than on the high  $M$  side, the footwall of the fault rotates and get uplifted more on the low  $M$  side. The footwalls along the ridge generates the isochron-parallel tectonic stress  $\sigma_{zz}$ . Since  $\sigma_{zz}$  follows

along the extending tip of the plastic strain and as <sup>EC:</sup>the extending tip of the plastic strain extends [What do you mean?],  $\sigma_{zz}$  also <sup>EC:</sup>extends [What do you mean by a stress component “extends”?]. Extending tip of the plastic strain together with  $\sigma_{zz}$  generate tensile failure that extends away from the ridge axis and thus produces the linear corrugations that are parallel to the spreading velocity. Detail analysis along with simpler model experiments are given in the “Discussion” section.

<sup>EC:</sup> [These sentences would better fit in model comparison section or Discussion.]

Corrugations are observed in most of the models except for the constant M model M88ContT2 (Figure 13). Among the models that have corrugations, the timing, location and the regularity of the corrugations varies. For example, corrugations in M58SinT1 shows up  $\sim 45$  kyr at the lower M side ( $0.5 < M < 0.65$ ) (Figure 23.a)). However, corrugations in M28LinT1 shows up much later at  $\sim 240$  kyr at the lower M side ( $0.2 < M < 0.38$ ) (Figure 8.c). For M28LinT1, the corrugations are mostly formed at the lower M side ( $M < 0.5$ ) through time and they are less regular along the ridge ((Figure 8.h)). But the corrugations in M58SinT1 appear along the whole ridge and shows regularly alternative undulations with a wavelength of  $\sim 1$  km (Figure 23.c)).

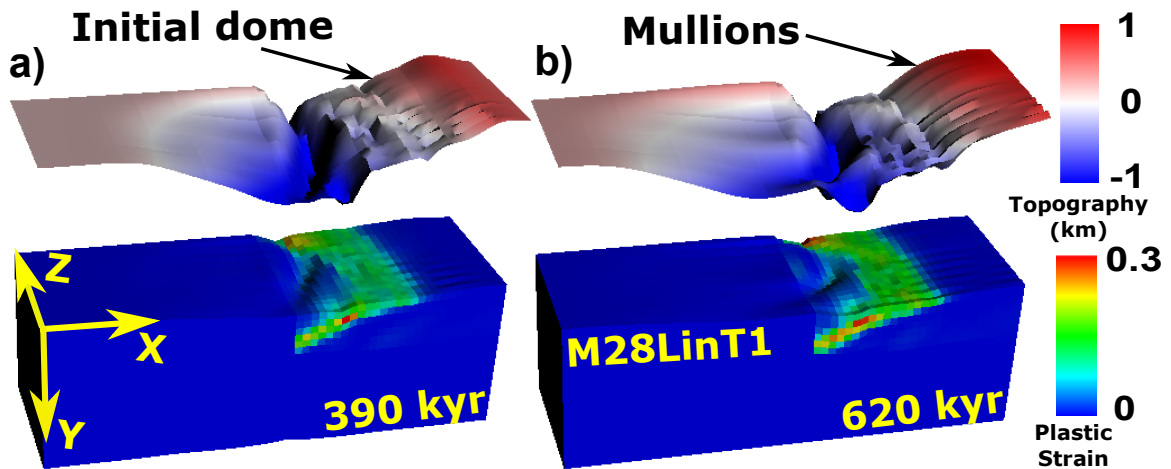


Figure 24: Evolution of mullion structures.

### Mullion structures

Mullion structures observed in the models are formed by the along ridge variation in the location of the termination due to the evolution of faulting. They usually appear at where the termination is closer to the ridge axis. The shape of the footwall follows the trace of the termination as it is exhumed to the surface. At where the termination is bent inward to the ridge axis, an “initial dome” (Figure 24.a)) is produced once the hanging wall is exhumed to the seafloor. The wavelength of the mullion structure is determined by the shape of the termination. If the pattern of the termination lasts for a long time and the footwall of the detachment fault keeps being exhumed to the surface following the trace of the detachment fault termination, a mullion structure is produced (Figure 24.b)).

### 3.3 Effects of the functional forms of M variation

#### 3.3.1 M28(Lin, Sin, Sqrt)T1

Comparing M28LinT1, M28SinT1 and M28SqrtT1, major differences lie in the model behaviors of the “inward fault jump”, the “cut-back” and the “hourglass shape median valley”. All three models have no fault alternation.

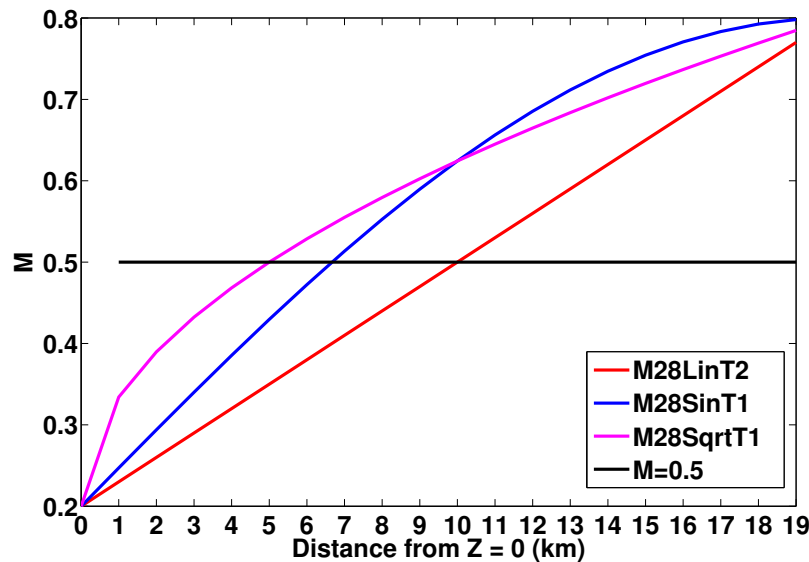


Figure 25: Three functional forms of M variation. M begins to exceed the  $M = 0.5$  black line at  $Z=10$  km, 7 km, 5 km for M28LinT1, M28SinT1 and M28SqrtT1 respectively.

## Inward fault jump

Only linear and sinusoidal models have inward fault jump. Square root model shows no inward fault jump because during cut-back, termination of the detachment fault retreats backward toward the ridge axis and the detachment fault is maintained near the ridge axis.

Between linear and sinusoidal models, timing and dimension of the inward jumping faults are different. For the linear functional form, the inward fault jump at the higher M side starts accommodating most of the extension at  $\sim 900$  kyr and replaces the initial detachment fault (Figure 26, Figure 8.f). It nucleates from the ridge center where  $M = 0.5$  and then propagates to the  $M = 0.8$  end with a length of  $\sim 11$  km. For the sinusoidal functional form, the inward fault jump takes the place of the initial detachment fault earlier at  $\sim 550$  kyr with a length of  $\sim 14$  km (Figure 26).

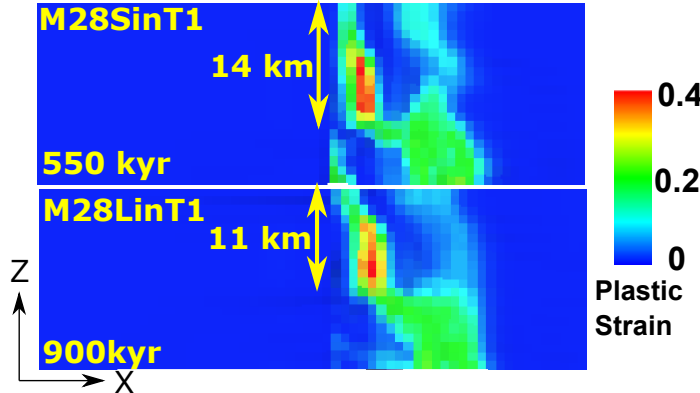


Figure 26: Bird's-eye view for comparing the length and timing of inward fault jump.

The timing difference between the linear and sinusoidal models is because M28SinT1 consistently has a higher M values than the M28LinT1 (Figure 25), which results in that the initial detachment fault at the higher M side ( $M > 0.5$ ) of M28SinT1 is pushed off axis faster than M28LinT1 and thus forming an earlier inward fault jump. The length difference is because M28SinT1 has a greater length along the ridge axis of  $M \geq 0.5$  (Figure 25).

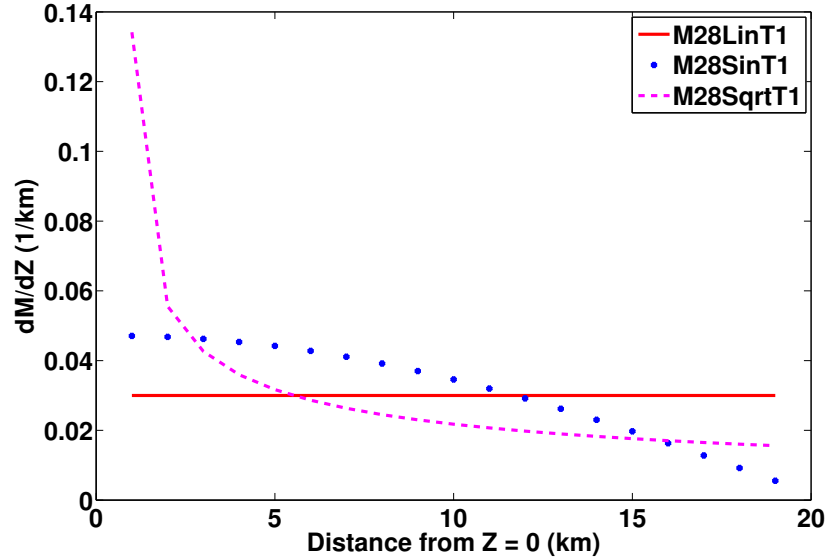


Figure 27:  $\partial M / \partial Z$  comparision.

### Cut-back

Cut-back only happens in the M28SqrtT1 model. Qualitatively, it is because M28Sqrt has a much higher value of  $\frac{\partial M}{\partial Z}$  at the lower M side (Figure 27), which implies a larger along ridge shear stress  $\sigma_{xz}$  as well as a larger difference in  $\sigma_{xy}$  along the ridge that result in the decoupling between the higher and lower M sides hanging walls.

### Hourglass shape median valley

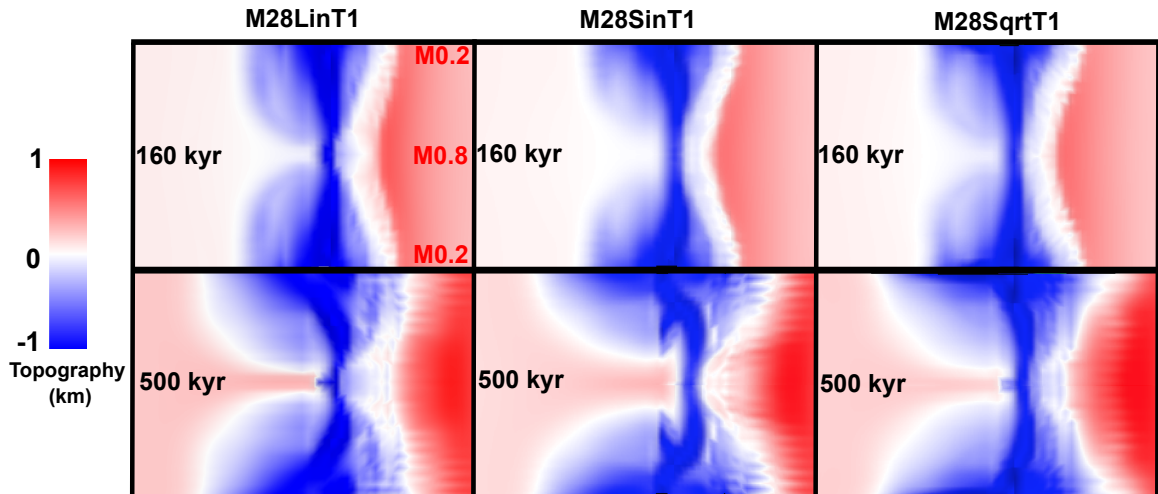


Figure 28: Bird's-eye view of the topography. (without vertical exaggeration.)

As shown in Figure 28, differences among the three models are identified. At 160 kyr, median valley for M28SinT1 has the smallest cross-section ( $x$ - $y$ ) area at the higher M side. While at the lower M side, M28SqrtT1 has the smallest area of the cross-section. This is because the cross-section area inside the median valley is inversely proportional to the local M value along the ridge. Moreover, the breakaways at the lower M sides for M28LinT1 and M28SinT1 bend to parallel to the ridge axis while the breakaway for M28SqrtT1 extends further away from the ridge axis. In addition, M28SinT1 has a trough inside the median valley with the highest curvature. At 500 kyr, M28SinT1 has the narrowest median valley at the higher M side and the high topography zone on the left hand side of the ridge axis is the widest. Integrating the topography at the left hand side of the ridge axis of the three models, M28Sqrt has the largest value of integration since it has the largest integration of M along the ridge axis. In addition, the termination of the detachment fault of M28SqrtT1 has the highest curvature at the lower M sides. All these observations correspond to the M variation (Figure 25).

### 3.3.2 M58(Lin,Sin,Sqrt)T2

Table 3: Average M values of the 20 km segment. (The value is calculated by integrating M along the ridge axis and divided by the length of the model domain in  $z$ -axis.)

M range Function	M28	M57	M58
Linear	0.4850	0.5950	0.6425
Sinusoidal	0.5668	0.6223	0.6834
Square root	0.5837	0.6279	0.6918

Among M58LinT2, M58SinT2 and M58SqrtT2, the major difference lies in whether it has “fault alternation”. Except for the constant M model M88ContT2, among all the models, only the models with type 2 weakening and M ranges from 0.5 to 0.8 (M58) have fault alternation. However, M58LinT2 does not produce alternating fault during the 1.1 Myr model time. Instead, one detachment fault lasts until  $\sim$ 300 kyr when the inward fault

jump happens at the higher M side ( $0.65 < M < 0.8$ ) and replaces the initial detachment fault. This provides an upper limit of average M value of the whole segment that prevent fault alternation and allows a long-lived detachment fault to produce a OCC. As shown in Table 3, the upper limit for the average M value is 0.6425 for M58LinT2. Detail analysis of the fault alternation is given in “Discussion”.

### 3.4 Effects of the weakening rate

Among the twelve 3D models, three pairs of models have both type 1 and type 2 weakening while the range of M and functional form are maintained to be the same. They are M57SinT1/T2, M58SinT1/T2 and M58SqrtT1/T2.

#### 3.4.1 M57SinT1 versus M57SinT2

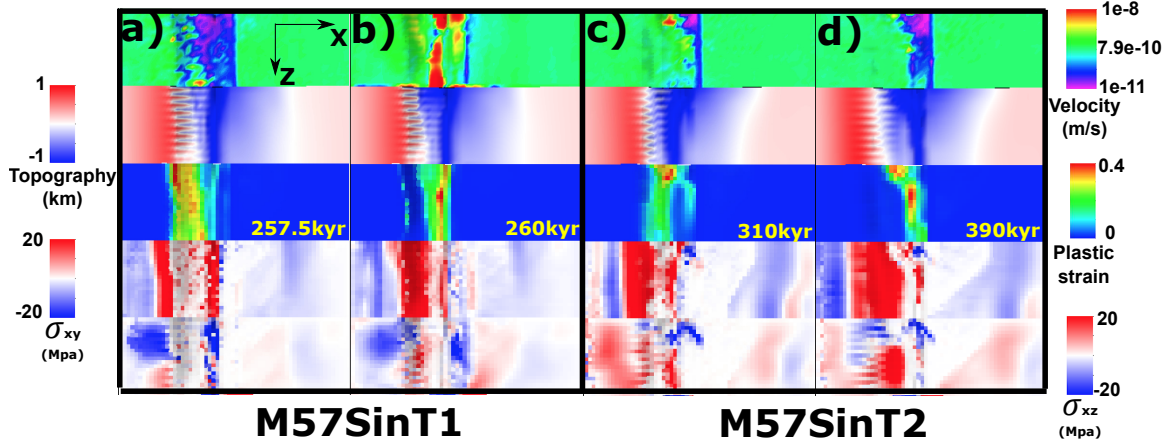


Figure 29: M57SinT2 versus M57SinT1 (Table 2)

Initially, both models develop normal faults on both sides of the ridge axis at the lower M side. In the model with the faster weakening rate (M57SinT1), faults propagate toward the higher M side and cut through the whole crust by 25 kyr but this process completes later by 50 kyr in the model with the slower weakening rate (M57SinT2). By  $\sim 310$  kyr, the inward fault jump appears at the higher M side ( $M > 0.55$ ) of M57SinT2 while at

where  $M \leq 0.55$ , the initial fault remains active (Figure 29.c and d). However, when the weakening is fast (M57SinT1), cut-back happens at  $\sim 260$  kyr and helps to maintain a relative higher angle fault with a termination closer to the ridge axis. The initial fault remains, no inward fault jump forming (Figure 29.a and b). In addition, the width of median valley at the lower M side is wider for M57SinT2 than M57SinT1 (Figure 29.c, d versus a, b) because slower weakening (type 2) allows a more distributed tensile stress  $\sigma_{xx}$  rather than fast weakening that once a fault establishes, larger amount of the tensile stress  $\sigma_{xx}$  is released at the fault. The amplitude of the corrugations of M57SinT1 is larger than that of slower weakening M57SinT2. This is because faster weakening rate allows a faster decrease in the cohesion. As the cohesion reaches its minimum of 4 MPa earlier when the plastic strain accumulates to 0.1, tensile failure is easy to happen in the isochron parallel direction and produces the corrugations.

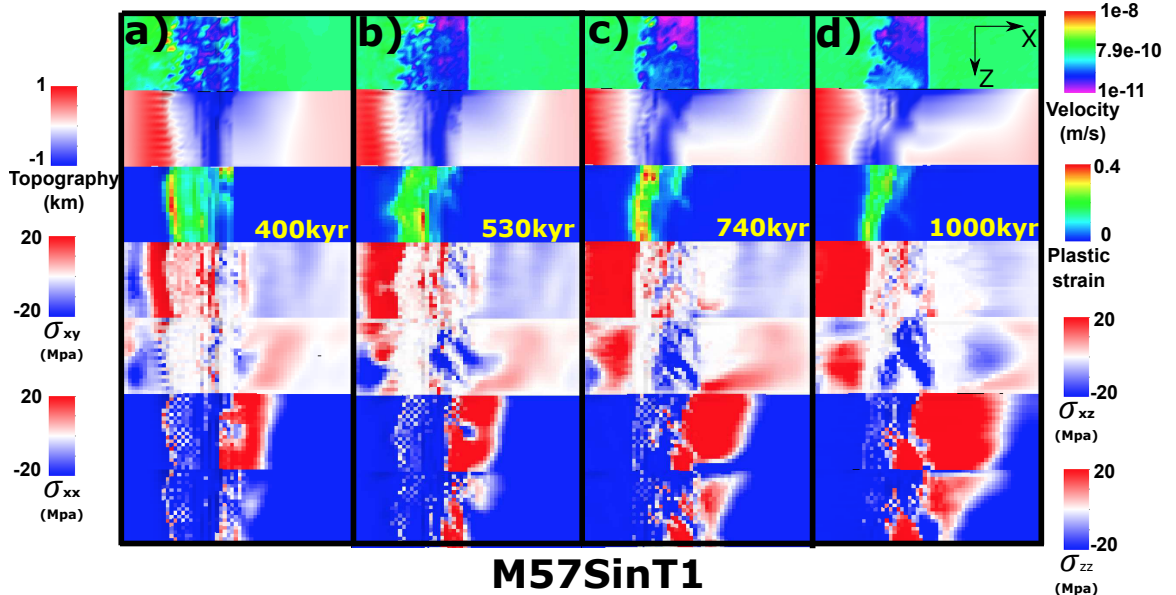


Figure 30: Faulting and stress evolution for M57SinT1.

### M57SinT1

For M57SinT1, by 400 kyr (Figure 30.a), two antithetic fault forms at the lower M side ( $0.5 < M < 0.58$ ) accommodating part of the plates extension. This makes the termi-

nation at the lower M side retreat backward to the ridge axis. The hanging walls of the antithetic faults slide down into the trough and lower the topography. By 530 kyr, the termination at the center of the ridge segment ( $M = 0.61\sim0.63$ ) extends further (Figure 30.b). This curved termination leads to a curved topography aligns with it (white curve in the second row). By 740 kyr, another antithetic fault forms at the lower M side (Figure 30.c). It doesn't take the place of initial fault and disappear soon, however, it again releases tensional stress and helps maintain a closer to ridge axis termination at the lower M side. By 1000 kyr (Figure 30.d), an Atlantiss Massif shape OCC is produced (lower M side has a wider dome and higher M side has a narrower dome) due to the along ridge termination evolution. Corrugations with wavelength varying from hundreds to kilometers are also produced.

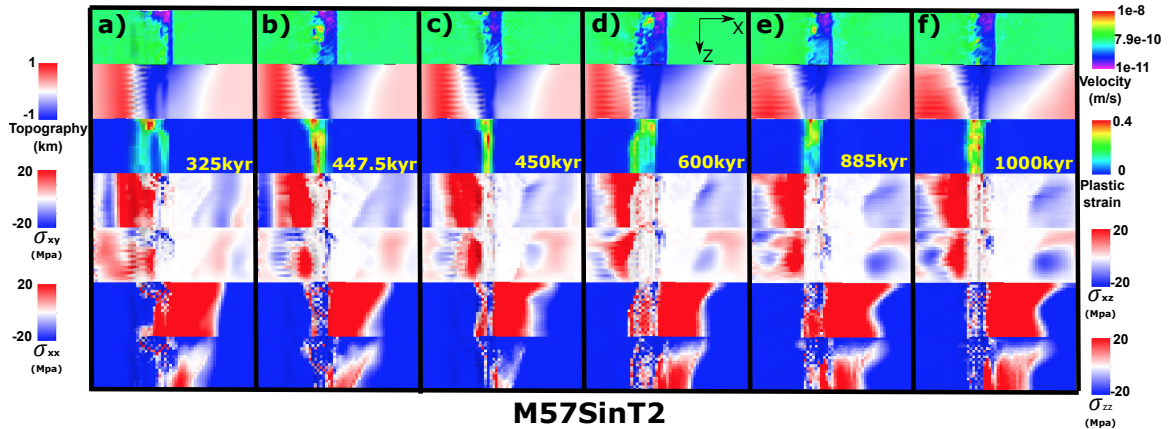


Figure 31: M57SinT2 (Table 2) faulting and stress evolution with respect to time.

## M57SinT2

For M57SinT2, instead of maintaining a detachment fault like M57SinT1, it produces inward fault jump at the higher M side. By 325 kyr (Figure 31.a), an inward fault jump happens and takes the place of the initial detachment fault at the higher M side. Between 447.5 kyr (Figure 31.b) and 450 kyr (Figure 31.c), a small scale cut-back happens and the termination recedes backward. By 600 kyr, the termination at the higher M side extends further (Figure 31.d). By 885 kyr, an inward fault jump happens at the higher M

side ( $0.62 < M < 0.7$ ) (Figure 31.e). The width of the median valley at the lower M side keeps increasing due to the distributed  $\sigma_{xx}$  (Figure 31.a~d).

### 3.4.2 M58SinT1 versus M58SinT2

A major difference between M58SinT1 and M58SinT2 is that only M58SinT2 has fault alternation.

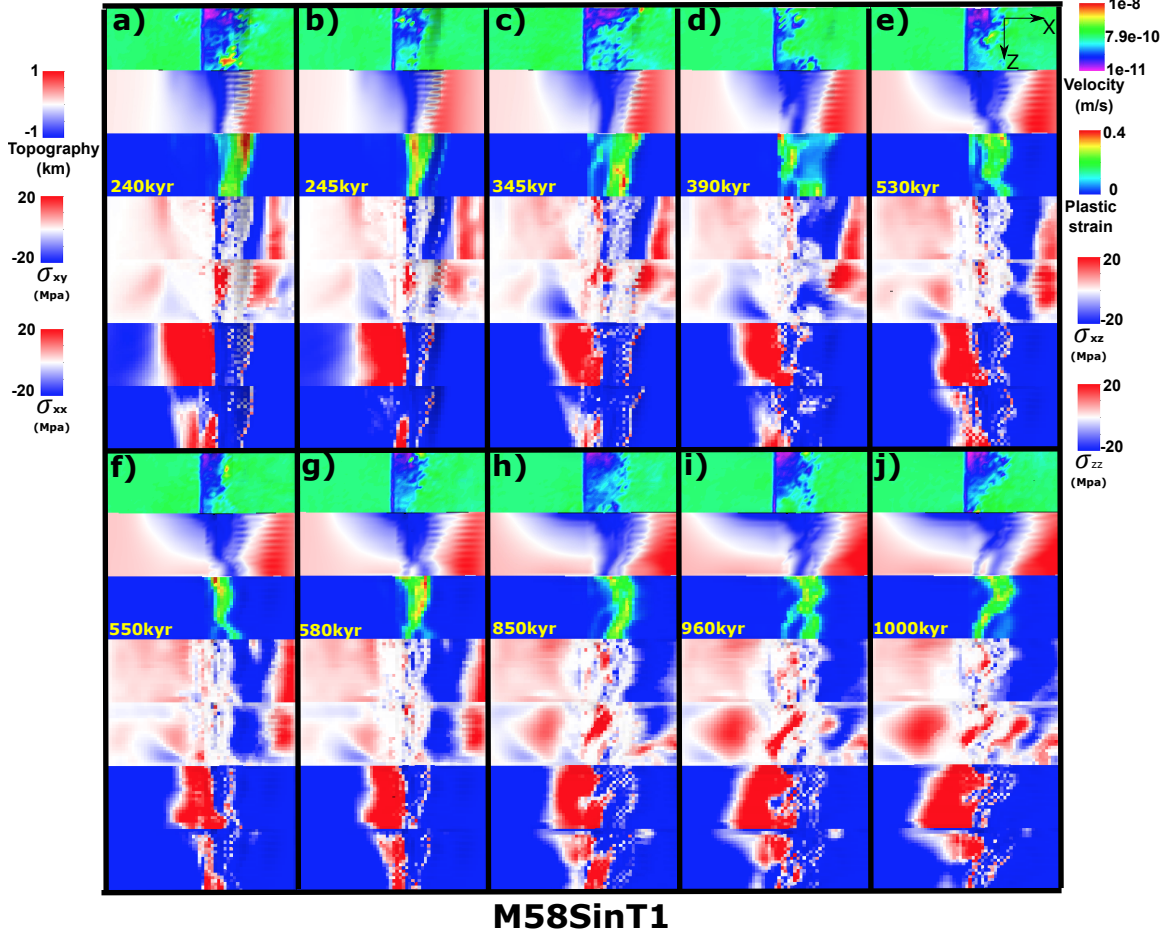


Figure 32: Faulting and stresses evolution (M58SinT1).

### M58SinT1

During the 1 Myr extension of the model M58SinT1, 10 phases of the evolution of faulting are identified (Figure 32.a~j). Antithetic faults, inward fault jumps, cut-backs happens and a rider block, corrugations and mullion structures are produced.

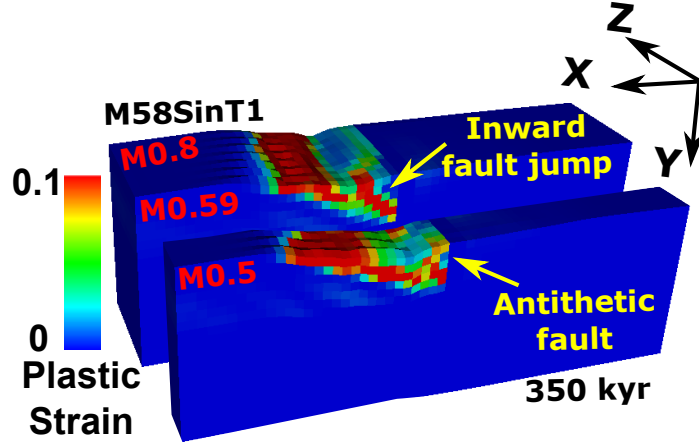


Figure 33: Plastic strain for M58SinT1 at 350 kyr.

By 240 kyr (Figure 32.a), due to fast weakening (type 1), cohesion along the termination is low. Stress  $\sigma_{zz}$  takes the advantage and generates  $\sim 2$  km wavelength corrugations parallel to the spreading direction as the termination extends further away from the ridge axis. Between 240 kyr (Figure 32.a) and 245 kyr (Figure 32.b), a cut-back happens with mass wasting at the lower M side. The termination recedes toward the ridge axis during the cut-back. By 345 kyr (Figure 32.c), an antithetic fault forms at the lower M side ( $0.5 < M < 0.545$ ) with an inward fault jump happens at at ridge segment with  $M \in (0.575, 0.635)$  (Figure 33). 45 kyr later, the two weak zone connect to each other and take the place of the initial detachment fault at the lower M side (Figure 32.d). Due to this inward fault jump, a dextral  $\sigma_{xz}$  zone (blue area in the  $\sigma_{xz}$  panel) forms and is bounded by the termination of the inward fault jump near the ridge axis at the lower M side and the termination of the initial detachment fault at the higher M side. By 530 kyr (Figure 32.e), the termination of the inward fault jump at the lower M side evolves to a curve with its center extends further away from the ridge axis because the inward fault jump initiates at the center and starts extending away from the ridge axis earlier, however, the lower M side of the curve remains closer to the ridge axis due to the antithetic fault and the other end of the curve is also closer to the ridge axis because the fault initiates later. This curved termination at the lower M side also connects to the initial detachment fault at the higher M

side which is further away from the ridge axis. Together, the curved termination is like a mirror reflected letter “S”. This flipped “S” shape termination is also reflected in topography. As the curved termination at the higher M side lasts for  $\sim 300$  kyr since  $\sim 390$  kyr, following the shape, a  $\sim 10$  km in wavelength and  $\sim 7$  km in along spreading direction mullion structure is formed (Figure 34). By  $\sim 680$  kyr, an inward fault jump happens at the higher M side ( $0.74 < M < 0.8$ ). It perturbs the curved shape termination and ceases the further exhumation of the mullion structure. This inward fault jump also produces a rider block that covers the inactive detachment fault and moves off axis following the exhuming footwall of the inward jumped fault.

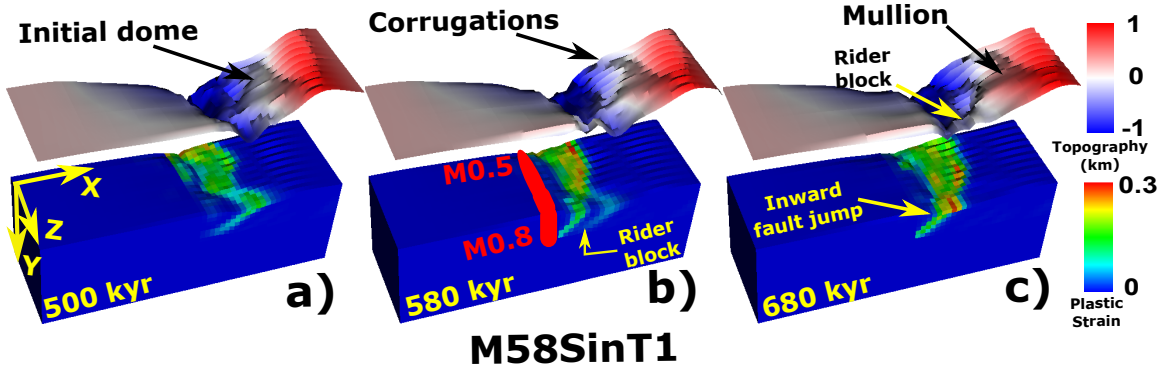


Figure 34: Evolution of faulting and morphologies of M58SinT1.

Between 530 kyr (Figure 32.e) and 550 kyr (Figure 32.f), another cut-back happens at the lower M side ( $0.5 < M < 0.545$ ) where a slump block with an area of  $\sim 9$  km $^2$  flows down the topography slope into the trough. Terminations recedes backward to the ridge axis. By 580 kyr, termination at the lower M side extends further away from the ridge axis due to less magma supply. Between 580 kyr and 850 kyr, due to two antithetic faults at the lower M side ( $M \in (0.5, 0.53) \cup (0.56, 0.605)$ ), the termination at the lower M side recedes and the previous mirror reflected “S” shape termination evolves to a half circle curve (Figure 32.h). The shape is also reflected in the topography. By 960 kyr (Figure 32.i)), at the ridge segment with  $M \in (0.62, 0.665)$ , another inward fault jump replaces the detachment fault away from the ridge axis and retreats the termination backward to the ridge axis forming two half circle curves with wavelengths of around half

of the model domain in  $z$ -axis. A large sinistral shear zone (red region  $\sim 40^\circ$  oblique to ridge axis) is seen in the  $\sigma_{xz}$  panel. The shear stress  $\sigma_{xz}$  results from the inward fault jump at the center of the ridge segment that previous hanging wall changes to the footwall of the inward jumped fault and generates a offset between the old hangingwall at the lower M end and the new footwall of the inward jumped fault. By 1000 kyr, due to the along ridge coupling, the inward fault jump propagates to the higher M side (Figure 32.j).

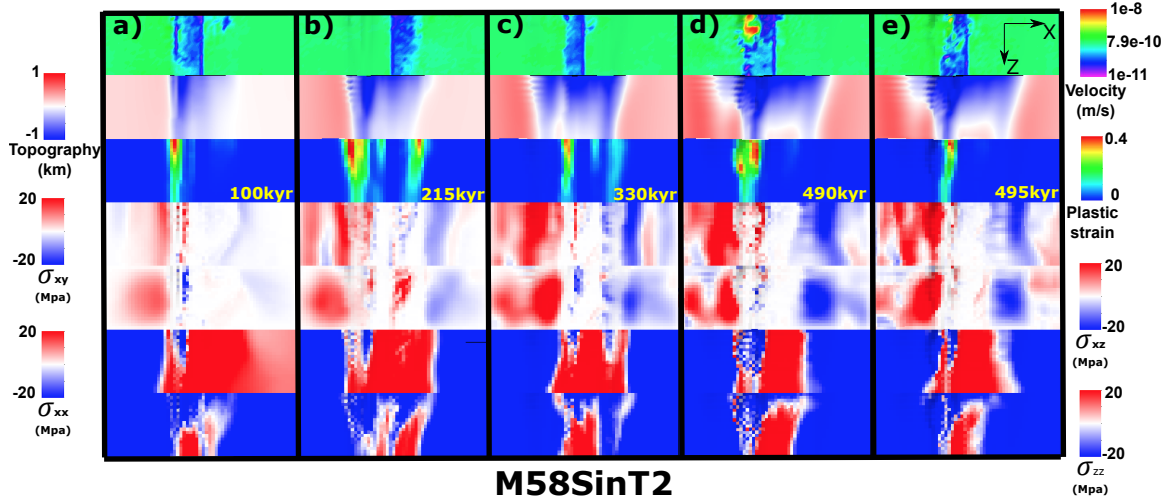


Figure 35: Faulting and stresses evolution of M58SinT2.

## M58SinT2

As shown in Figure 35, a fault initiates on the left hand side of the ridge axis (Figure 35.a). The breakaway at the lower M side extends further than that of the higher M side. It takes longer time of  $\sim 100$  kyr to form a localized fault plane through the whole ridge segment due to the slower rate of weakening (type 2). By 215 kyr (Figure 35.b), fault alternates to the conjugate plate and gradually replaces the initial one. Corrugations are only produced at the lower M side ( $M \in (0.5, 0.62)$ ). By 330 kyr, fault alternates again. Between 490 kyr (Figure 35.d) and 495 kyr (Figure 35.e), a cut-back happens with mass wasting and termination receding. A slump block of an area of  $\sim 16$  km $^2$  flows down the topography slope into the trough. With fault alternation, the shape of the median valley is no longer an hourglass. However, at the lower M side, the median valley is still

wider and deeper. High frequency abyssal hills are produced at the higher M side. In addition, M58SinT2 has a fault alternation frequency of  $\sim 150$  kyr which is higher than that of M88ConT2. <sup>XT</sup>Reason for this difference needs further discussion.

### 3.4.3 M58SqrtT1 versus M58SqrtT2

The major difference between M58SqrtT1 and M58SqrtT2 is also whether the normal fault alternates or not.

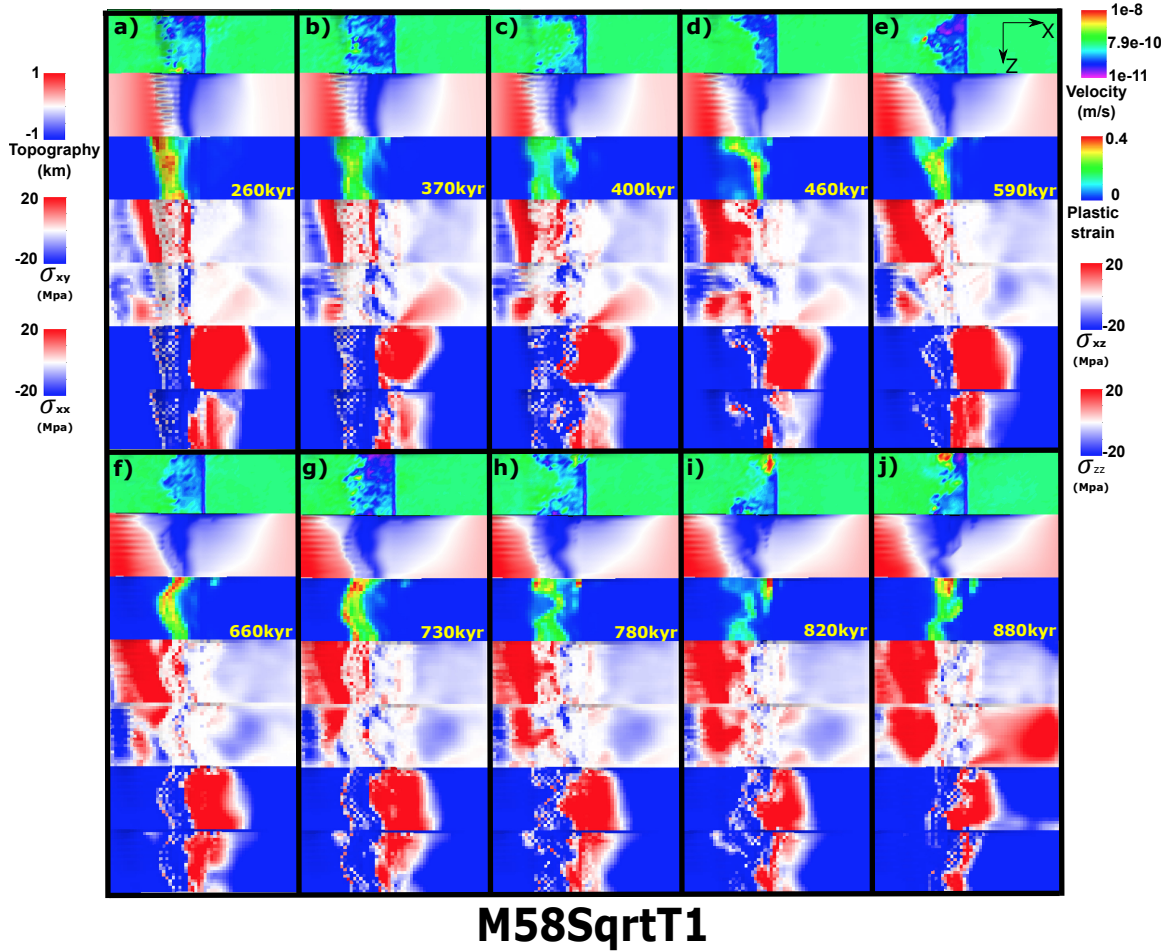


Figure 36: M58SqrtT1 (Table 2) faulting and stress evolution with respect to time.

### M58SqrtT1

By 260 kyr, breakaway at  $M = 0.5$  extends  $\sim 5$  km further away from the ridge axis than that of the higher M end (Figure 36.a). Corrugations of a wavelength of  $\sim 2$  km <sup>XT</sup>2

km is the correct wavelength for corrugations, change previous wrong ones of 1 km are produced along the ridge. By 370 kyr (Figure 36.b), due to larger value of  $\frac{\partial M}{\partial Z}$  at the lower M side, a vertical tensile failure takes place at  $M \in (0.5, 0.5949)^{XT}$ . previous M range for Sin and Sqrt models should be revised, I used linear to calculate with respect to number of elements in Z. Start from this and the later ones are ok. Two parallel dextral shear stress zones (blue) are seen in the  $\sigma_{xz}$  panel. By 400 kyr (Figure 36.c), an inward fault jump happens at where  $M \in (0.5949, 0.7121)$  and it propagates to the higher M end and replaces the initial detachment fault at the higher M side by 460 kyr (Figure 36.d). By 590 kyr (Figure 36.e), an inward fault jump happens at the lower M side ( $M < 0.5949$ ) and connect with the normal fault at the higher M side replacing the initial detachment fault. An  $\sim 18 \text{ km}^2$  triangular shape (bird's-eye view) rider block is produced at the lower M side. Termination at the center of the ridge segment extends furthest away from the ridge axis. This is because the previous inward fault jump first initiates there, so the fault starts slipping earlier and because the value of M is lower at the segment center than the higher M end. By 660 kyr (Figure 36.f), as the previous inward jumped fault at the higher M side evolves, another dome is produced. There is a hint of high angle normal fault at where  $M < 0.5949$  on the conjugate plate. But it doesn't develop. By 730 kyr (Figure 36.g), the termination evolves to a "half circle" and the shape is also seen in the topography. By 780 kyr (Figure 36.h), another inward fault jump appears at the ridge segment with  $M \in (0.6342, 0.7121)$  and produced a curved termination with a wavelength of  $\sim 10 \text{ km}$ . It has the potential to create a large wavelength mullion structure. Meanwhile, at the lower M side ( $M < 0.5949$ ) near the ridge axis, an antithetic fault forms and propagates toward the higher M side (Figure 36.i). It triggers another inward fault jump to happen at the lower M side and produces another rider block. The inward jumped fault later connects with the detachment fault at the higher M side (Figure 36.j). In addition, a tensile failure shows its hint at the lower M side ( $M < 0.6342$ ) of the conjugate plate.

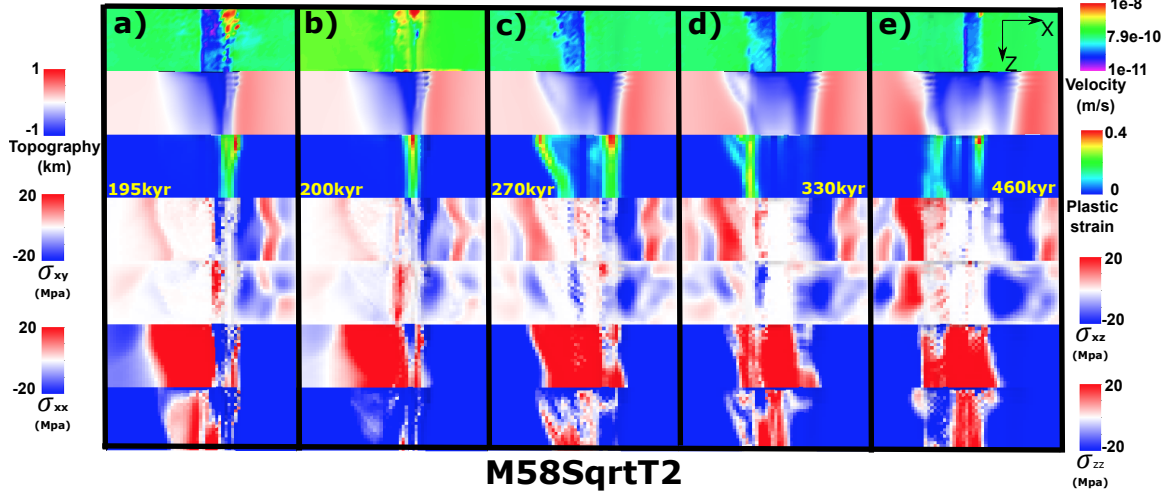


Figure 37: Faulting and stresses evolution for M58SqrtT2.

### M58SqrtT2

By 195 kyr (Figure 37.a), breakaway at the lower M side extends further away from the ridge axis. Three corrugations begin to show up due to tensile failure. Median valley on the conjugate plate is wider at the lower M side because slow weakening allows a more distributed  $\sigma_{xx}$  that results in the elastic depression of the conjugate plate. Between 195 kyr (Figure 37.a) and 200 kyr (Figure 37.b), a cut-back happens with mass wasting along the ridge and is followed by the termination retreat. By 270 kyr fault alternates (Figure 37.c). The shape of the alternated fault follows the curved shape shear  $\sigma_{xy}$  zone (red) as seen since  $\sim 195$  kyr on the left hand side of the ridge axis. By 330 kyr (Figure 37.d), at the lower M side, an inward fault jump happens and takes the place of the old fault further away from the ridge axis. By 460 kyr (Figure 37.e), fault alternates again to the right hand side of the ridge axis.

### 3.5 Effects of the range of M variation

Generally, M57 and M58 models create a median valley much narrower and shallower than that of M28 models.

### 3.5.1 (M28 M57 M58)SinT1

#### M57SinT1 versus M58SinT1

For description of M57SinT1 evolution with respect to time, please refer to Section 3.4.1 and Figure 30. For description of M58SinT1 evolution with respect to time, please refer to Section 3.4.2 and Figure 32. Comparing M57SinT1 and M58SinT1, the major difference is that the faulting pattern evolution for M58SinT1 is much more dynamic with a higher frequency of inward fault jumps, cut-backs and connection of the offsetted fault zones. For M58SinT1, the inward fault jumps and antithetic faults usually replace the old ones. However, for M57SinT1, diking is not strong enough to create big enough stress perturbation along the ridge axis for inward fault jumps or antithetic faults to take the place of the original one. At the lower M side, antithetic faults only help to accommodate tensional stress which assists in maintaining a termination near the ridge axis while the termination at the higher M side gradually moves off axis. This produces an OCC with larger dome at the lower M side than that of higher M side which is opposite to the shape of the OCC produced by M58SinT1.

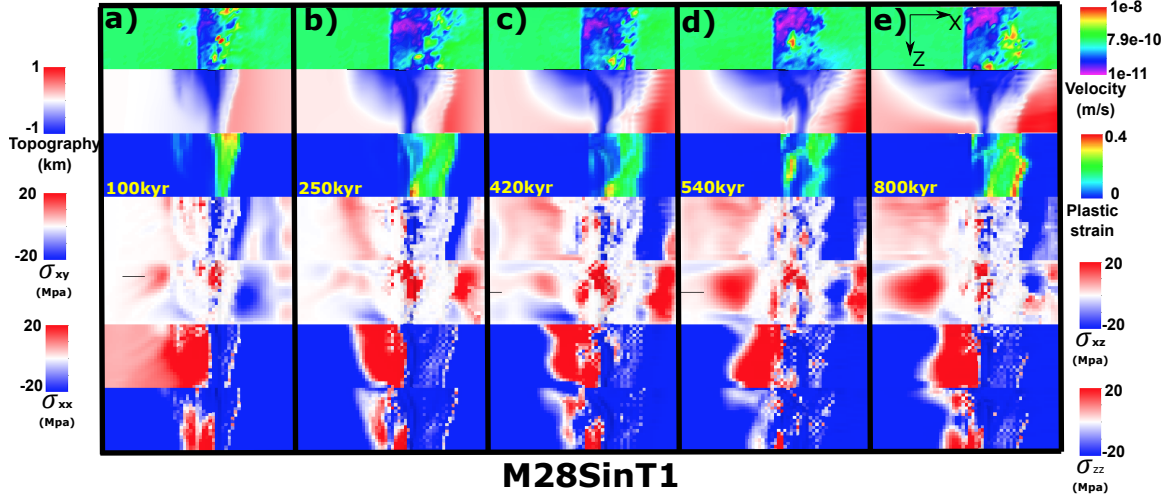


Figure 38: M28SinT1 (Table 2) faulting and stress evolution with respect to time.

#### M28SinT1

As shown in Figure 38, faulting evolution is much less dynamic than that of M58SinT1. One detachment fault keeps active on the right hand side of the ridge axis. Only inward fault jump happens  $\sim$ 540 kyr (Figure 38.d). By  $\sim$ 100 kyr (Figure 38.a), breakaway at the lower M side extends  $\sim$ 4 km further away from ridge axis than the higher M side. By 250 kyr (Figure 38.b),  $\sim$ 4 corrugations begin to evolve at the lower M side ( $M \in (0.2, 0.5135)$ ). By 420 kyr, at the higher M side, a hint of inward fault jump begins to show up. It develops into an inward fault jump by 540 kyr (Figure 38.d) and propagates toward higher M side. At the lower M side ( $M \in (0.2, 0.2939)$ ), a tensile failure takes up part of the plate extension and helps maintain a closer to ridge axis termination than the extending termination at the region with  $M \in (0.4724, 0.6562)$  (Figure 38.e). The curved in termination at the lower M side produces a mullion structure.

### 3.5.2 M57SinT2 versus M58SinT2

For description of M57SinT2 evolution with respect to time, please refer to Section 3.4.1 and Figure 31. For description of M58SinT1 evolution with respect to time, please refer to Section 3.4.2 and Figure 35. A major difference is that M57SinT2 has no fault alternation while M58SinT2 has.

### 3.5.3 M28LinT1 versus M57LinT1

For description of M28LinT1 evolution with respect to time, please refer to Section 3.1.

#### M57LinT1

As shown in Figure 39, between 160 kyr (Figure 39.a) and 162.5 kyr (Figure 39.b), a cut-back happens. The corrugations have a relatively high amplitude. Due to less M variation (0.2), the along ridge offset in breakaways is smaller. The median valley almost has a constant width along the ridge. By 350 kyr (Figure 39.c), a tensile failure happens at the region with  $M \in (0.5, 0.61)$  and generates a linear topography low. Another shorter

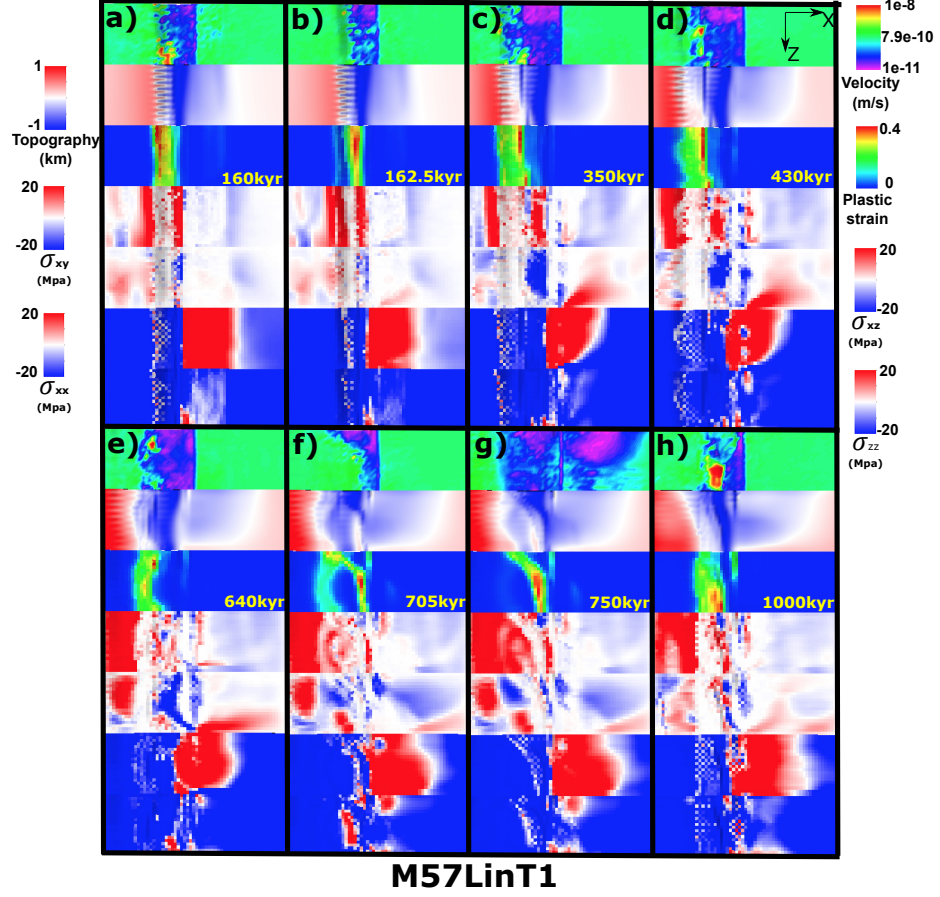


Figure 39: M57LinT1 (Table 2) faulting and stress evolution with respect to time.

tensile failure at the higher M side ( $M > 0.64$ ) helps maintain a high angle normal fault near the ridge axis. By 430 kyr (Figure 39.d), the tensile failure at the lower M side ( $M < 0.52$ ) is responsible for the retreat of the termination. While at where  $M \in (0.54, 0.59)$ , the termination extends further away from the ridge axis. This curved termination results in a “dog bone” shape topography as seen at 640 kyr (Figure 39.e) and is also responsible for the large dextral shear (blue) stress  $\sigma_{xz}$ . By 705 kyr (Figure 39.f), an inward fault jump happens and replaces the original detachment fault at the higher M side with a length of  $\sim 15$  km. This inward jumped fault connects with the detachment fault at the lower M side. The new “L” shape termination is responsible for the topography seen at 1000 kyr (Figure 39.h). The termination at the higher M side soon catches up the further extended termination at the lower M side due to the presence of a tensile failure.

### **3.5.4 M28SqrtT1 versus M58SqrtT1**

For description of the evolution of M28SqrtT1, please refer to Paragraph 3.2.5. For description of evolution of M58SqrtT1, please refer to Paragraph 3.4.3. Generally the faulting evolution for M58SqrtT1 is more dynamic with several inward fault jumps, antithetic faults, connection between offseted faults along the ridge while M28SqrtT1 is simpler with only two cut-backs.

### **3.5.5 M57SqrtT2 versus M58SqrtT2**

For description of evolutio of M58SqrtT2, please refer to Paragraph 2.

The major difference between M57SqrtT2 and M58SqrtT2 is that only M58SqrtT2 has fault alternation.

#### **M57SqrtT2**

For M57SqrtT2, six small scale cut-back happen at 282.5 kyr, 290 kyr, 365 kyr, 452.5 kyr, 482.5 kyr and 540 kyr respectively. As shown in Figure 40, the fault keeps on the left hand side of the ridge axis. By 200 kyr (Figure 40.b), an inward fault jump begins to evolve and takes the place of the initial fault. As the fault evolves, a stage of discontinuous abyssal hill is produced at the lower M side (Figure 40.c). The fault propagates toward the higher M side and cuts through the plate by ~245 kyr (Figure 40.d) when corrugations at the lower M side are produced. Between 365 kyr (Figure 40.e) and 367.5 kyr (Figure 40.f), a cut-back happens. By 490 kyr (Figure 40.g), an antithetic fault begins to evolve and terminates the old fault. It then develops into a vertical tensile failure at 540 kyr (Figure 40.h). XT:for M57SqrtT2, the topography since 200 kyr uplifted, I suspect ther might be some runtime error for this model. Consider to abandon this model and if possible, rerun it.

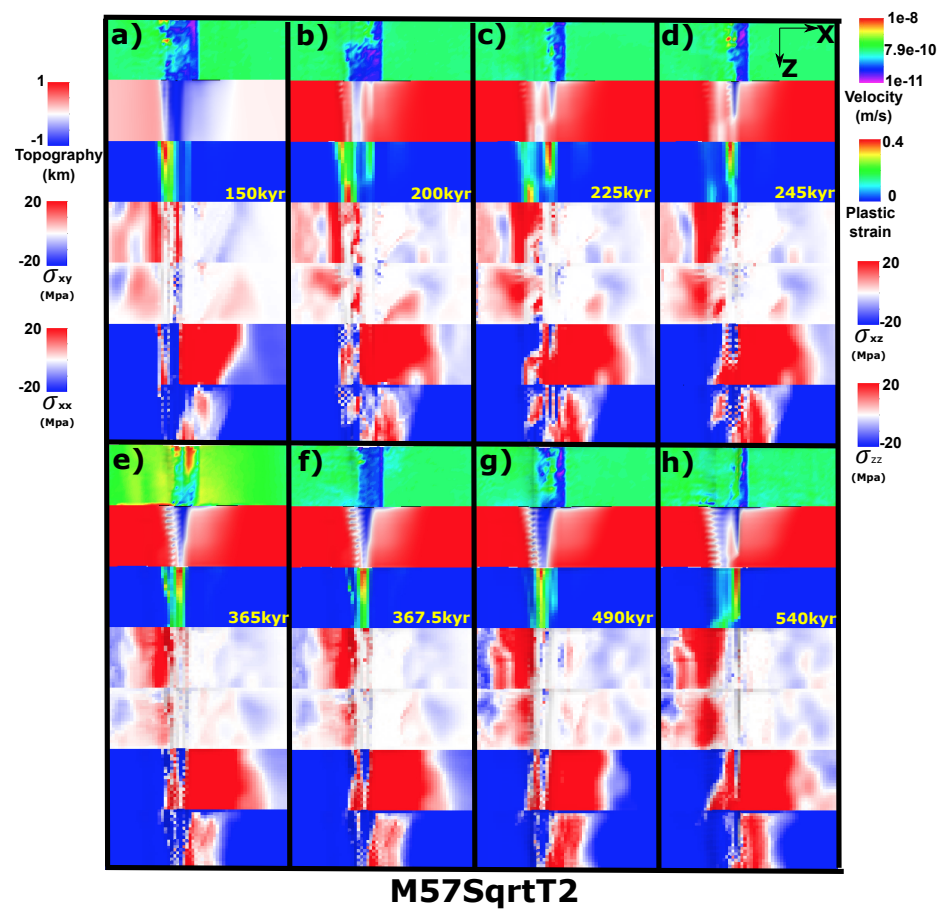


Figure 40: M57SqrtT2 (Table 2) faulting and stress evolution with respect to time.

## 4 Discussion

### 4.1 Summary of Results

There are several behaviors that are controlled by the model parameters. Generally, only M58 models with type 2 weakening produce alternating faults on both side of the ridge axis. All the models show corrugations. As for faulting patterns in terms of evolution frequency, usually Square root is more dynamic than Sinusoidal than Linear, M58 is more dynamic than M57 than M28.

Following tables are a summery of the model behaviors with respect to different setup parameters.

Table 4: Model behaviors in short.

A	Alternating Fault	C	Corrugation	SL	Shear Topography Low
NA	Not Alternating	SF	Secondary Fault on one side	CB	Cut Back
DD	Double Dome	AM	Atlantis Massif Shape		

Based on the 11 models with M variation, we observed eight first-order behaviors as shown in Table 4.

Table 5: Linear functional form.

M range Type \ Type	M28	M57	M58
Type one	NA; C; SL; SF <sub>1500 kyr</sub> ; DD	NA; C; SF <sub>1380 kyr</sub> ; CB <sub>330 kyr</sub> ; AM(opposite z)	
Type two			

Generally, all models forms a median valley that deepens and widens toward the lower M side (Figure 8) except the reference model with constant M= 0.8 (Figure 13). The topography obseved in our models, to the first order, is controlled by the spatial and temporal distributions of faulting and to the second order, results from elastically deformation

Table 6: Sinusoidal functional form.

M range Type \	M28	M57	M58
Type one	NA; C; SL; SF <sub>995kyr</sub>	NA; C; SL; SF <sub>760kyr;1320kyr</sub> ; CB <sub>520kyr</sub> ; AM	NA; C; SL; CB <sub>510kyr</sub> ; SF <sub>760kyr;1140kyr;1990kyr</sub>
Type two		NA; C; SL; SF <sub>680kyr</sub> ; CB <sub>905kyr</sub>	A <sub>450kyr;600kyr</sub> ; C(only at low M); CB <sub>990kyr</sub>

Table 7: Square root functional form.

M range Type \	M28	M57	M58
Type one	NA; C; SL; CB <sub>205kyr;330kyr;1025kyr</sub>		NA; C <sub>1770kyr</sub> (due to shear with dif wave length); SF <sub>860kyr</sub> (high M); SF <sub>1190kyr</sub> (low M)(Dog Bone); SF <sub>1690kyr</sub>
Type two		NA; C; SF <sub>435kyr;1060kyr</sub> ; CB <sub>585kyr</sub> ; CB <sub>735kyr</sub> ; CB <sub>910kyr</sub> ; CB <sub>970kyr</sub>	A <sub>550kyr;920kyr</sub> ; C; CB <sub>400kyr</sub>

(e.g. The gradual deepening and widening of the median valley; The bending of the crust at the footwall side of the detachment fault results in a domal shape of the fault interface as a mechanism for producing the dome shape of OCCs).

The pattern of the deformation (faulting and elastic deformation) is controlled by the evolving stress in the crust in terms of its distribution and magnitude. The stress evolution is a result of the interaction processes between tectonics and magmatism. Due to constant seafloor spreading, tensional stress orthogonal to the ridge-axis in the crust keeps accumulating. At the same time, along ridge-axis varying diking partially accommodates the stress from far field extension and perturbs the homogeneity state of stress distribution along the ridge-axis. Accumulated stress will be largely released when the tensile or shear failures establish.

Since the model behavior is very complicated. We will focus on the effects being

brought by the along ridge-axis variation in diking. Thus, it is worth considering a thought experiment with two end members: One, the along ridge-axis coupling is rigid, so that even along ridge axis variation in  $M$  exist, once a fault determined to develop, it will cut through the whole model domain along the ridge-axis(Z-axis) simultaneously. The other end member is that there is totally no coupling along the ridge-axis. So that each slice of crossection profile across the ridge behave separately without being influenced by its neighbour to a extreme that the model behavior is just a combination of 20 pseudo-2D models piled up along ridge-axis with their own  $M$ . (IMPORTANT: this suggests the importance and urgance for making clear conclusion and results description for previous pseudo-2D models results. However, one difficulty here is that the characteristic fault offset  $\Delta X_c$  is different between 2D and 3D models.)

## 4.2 Fault Alteration

### 4.2.1 Trade-off between bending and weakening

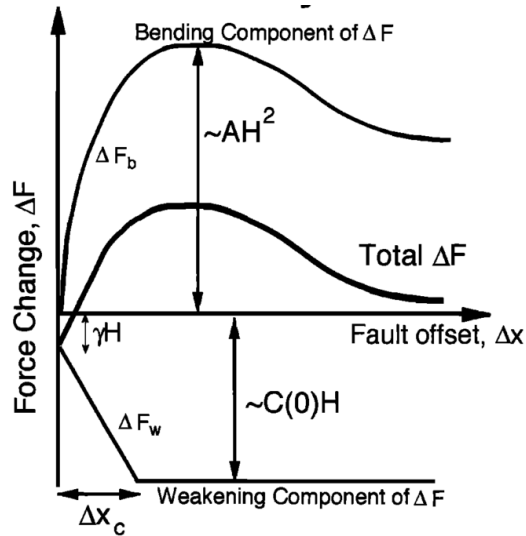


Figure 41: Trade-off between change in bending force  $\Delta F_b$  and weakening in the fault interface  $\Delta F_w$ .  $H$  is the thickness of the brittle crust and  $\gamma$  is the size of initial weak perturbation and  $A$  defines the maximum bending force change. (For more details, please refer to [Lavier et al., 2000])

Before we move on to each of the pairs, the framework studied by [Lavier et al., 2000] needs to be mentioned here for better understanding the model behaviors observed in our model results. There is a trade-off between change in bending force  $\Delta F_b$  as a function of fault offset  $\Delta X$  and force change  $\Delta F_w$  as a function of  $\Delta X$  due to strain weakening. As described in [Lavier et al., 2000], higher characteristic fault offset ( $\Delta X_c$ ) or slower strain weakening results in multiple faults rather than only one fault lasting. Whether conjugate fault and even multiple faults can be produced depends on the local stress condition. The strength weakening of the existed fault combines with how much bending force resists the fault to keep offsetting play a major role in determining the stress state at the other areas. As the sea-floor keeps spreading and  $\Delta X$  increasing, the change in bending force  $\Delta F_b$  increases and the strength at the fault interface decreases due to weakening  $\Delta F_w$  (Figure 41). If the net force change  $\Delta F = \Delta F_b + \Delta F_w$  is positive, it means that it is getting harder and harder to maintain the existing fault and stress will begin to accumulate at the other areas which eventually break another fault.  $\Delta F_b$  initially increases fast with respect to  $\Delta X$  and then when the breakaway bends over, it reaches its peak value and begins to decrease a little and maintains at a constant value. If the strain weakening is fast enough that the net effect force  $\Delta F$  is always negative, then most of the stress will be released by the existing fault and thus no conjugate or multiple faults will be created.

Our model results verify this analysis that only Type two weakening (slower weakening with higher  $\Delta X_c$ ) can produce an alternating normal fault on the conjugate plate.

Based on the previous experience in pseudo-2D models and [Lavier et al., 2000], when  $M > 0.5$ , the frequency of normal faulting alternation is higher for higher characteristic fault offset ( $\Delta X_c$ ) of Type two weakening compared to Type one weakening. However, for the reference model two, M88ConT2 (Table 2), interesting enough, when comparing pseudo-2D and 3D models with Type two weakening under case of  $M = 0.8$ , even though the 3D Model has a larger  $\Delta X_c$  of 1km than that of pseudo-2D model of 0.5km, the 3D model M88ConT2 has a lower frequency of faulting alternation. Since  $M$

is constant 0.8 along the ridge-axis, the effect of along ridge coupling that resists alternation need not be considered. One possibility is that the resisting bending force increase in a higher rate than linear with respect to increasing the length of the ridge segment ( $Z_{max}$  km).

#### 4.2.2 Alternating on conjugate plate

The fault alternation behavior observed in pseudo-2D models in cases  $M > 0.5$  is much more complicated in 3D models. The results shows that only Type two weakening with M58 will result in a alternating faulting pattern. *XT: integrate the area of  $M > 0.5$  with respect to Z to see if there is any quantatative analysis available.*

#### 4.2.3 Secondary near-axis normal fault

The secondary near axis high angle normal fault is another common observation of the models. As shown in Figure 8, at the ridge axis with  $M > 0.5$  (i.e.  $Z > 10$ ), the existing normal fault will be pushed away from the ridge-axis due to excessive diking, as its mechanism has been mentioned in the introduction chapter, another new near axis normal fault is created at around 650kyr. As it evolve, the initial detachment fault become inactive (the transparent view of plastic strain shown in the rigth corner inset of time 880kyr). This secondary fault creates another dome and its composition is more likely to be volcanic rather than ultramafic, however, as is evolve, if it can last long, lower crust and upper mantle material can be exhumed to the surface. The composition of the domes observed at Kane magamullions is similar to this mechanism that ultramafic Babel dome is on the West and crustal inside-corner high on the East.

#### 4.2.4 Effect of along ridge-axis coupling

The along ridge-axis coupling allowed the normal fault at the high M side ( $M > 0.5$ ) to last for a long time and become a detachment that can produce a OCC. This behavior is

different from previous 2D studies that only  $M=0.3 \sim 0.5$  can make OCCs and it also provides an alternative explanation for reconciling the gap between 2D model and observation described in [Olive et al., 2010]. Instead of magma injecting below brittle dutile transition, even injecting in the crust, due to along ridge coupling, model can still create OCC for high magma supply. Find the observation evidence for high M OCC from refs of Olive2010. As mentioned in the abstract of Olive2010, ref4-11 show a spectrum of magma supply.

### 4.3 Corrugations

There are two contributing factors, for one, trans-extenstional stresses are created due to offset of the breakaway as well as the variation in fault displacements along the ridge axis; for the other, the variation of the positions of the terminations of the detachment faults along the ridge-axis creates anastomosing faults that is mentioned in [Smith et al., 2014]. This anastomosing faulting behavior is largely responsible for corrugations in our models.

The stress at the tips of the breakaways is generally tensional in both parallel and orthogonal directions to the ridge-axis. (Figure ??f,g)

#### 4.3.1 Wavelength of corrugations

### 4.4 Influence of healing

### 4.5 Comparing model results with nature observation

#### 4.5.1 Cut back at 13°N Mid-Atlantic Ridge (M28SqrtT1)

The cut back behavior in M28SqrtT1 model creates a fault scarp of  $\sim 1\text{km}$  in relief, 40km in length along the Z axis. Note that the fault scarp corresponds to initial formed break-away. The topography at 13°N Mid-Atlantic Ridge also has a fault scarp with very similar

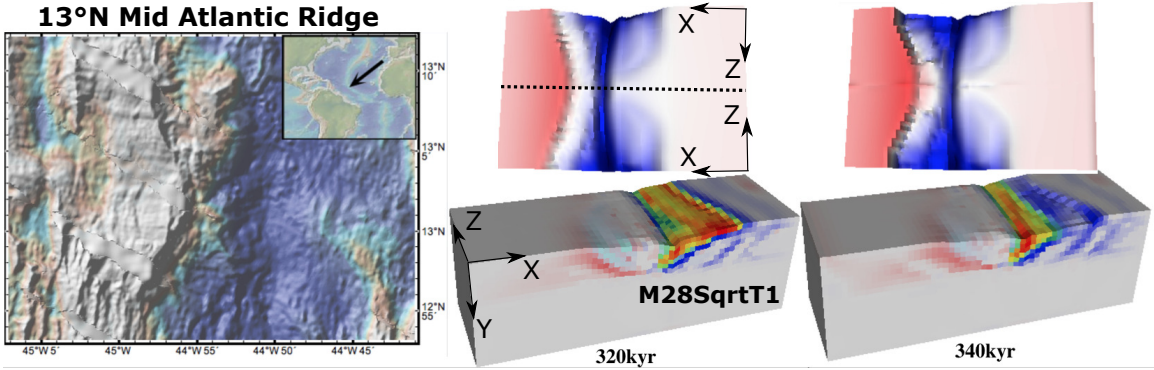


Figure 42: Comparing nature observation at 13°N Mid-Atlantic Ridge to the Cut back behavior of model M28SqrtT1. The model topography is a mirror symmetric flip according to the dash line, it reveals the case of  $M$  varies in a square root functional form from 0.2 to 0.8 to 0.2. For discussion on cut back formation mechanism, please refer to Section ???. The bathymetry is from GeoMapApp [Ryan et al., 2009].

geometry with  $\sim 1\text{km}$  in relief. Due to the variation in diking along the ridge-axis, a sandglass shape of median valley is also produced in the model where the narrowest center corresponds to the region with high magma supply ( $M=0.8$ ). This sandglass shape is also frequently observed in the nature along the Mid-Atlantic Ridges.

#### 4.5.2 Double dome at 23°N Mid-Atlantic Ridge (Kane Megamullions) (Several models)

#### 4.5.3 Atlantis Massif Shape at 30°N Mid-Atlantic Ridge ()

#### 4.5.4 Shear low

#### 4.5.5 Corrugations

### 4.6 Model Limitation

#### 4.6.1 Fixed thermal structure effects and justification

Thermal conduction rate for  $\kappa = 6\text{mm}^2/\text{s}$  material is  $1.8\text{e}5 \text{ km/Myr}$ , four magnitude faster compared to spreading rate of  $2.5\text{km/Myr}$ .

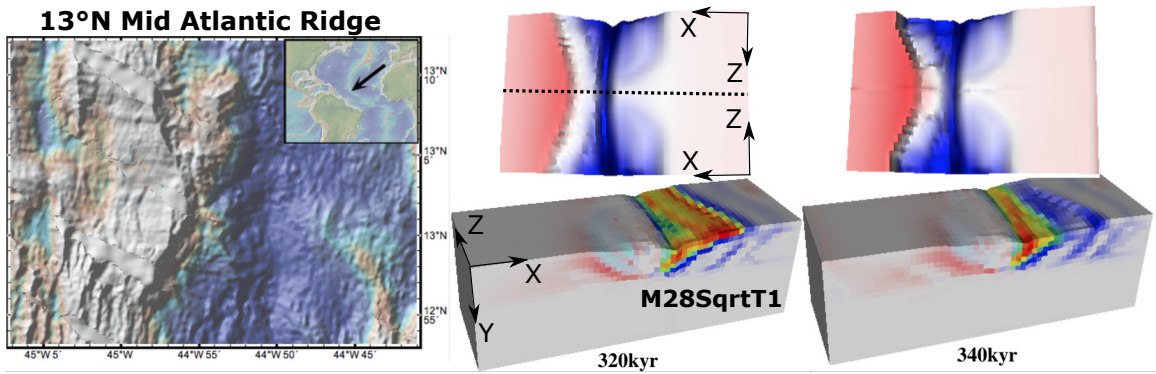


Figure 43: Comparing nature observation at  $13^{\circ}\text{N}$  Mid-Atlantic Ridge to the Cut back behavior of model M28SqrtT1. The model topography is a mirror symmetric flip according to the dash line, it reveals the case of  $M$  varies in a square root functional form from 0.2 to 0.8 to 0.2. For discussion on cut back formation mechanism, please refer to Section ??.

## 4.7 Recommendation for Future Research

## **5 Conclusions**

## Bibliography

- G. Baines, M. J. Cheadle, B. E. John, and J. J. Schwartz. The rate of oceanic detachment faulting at atlantis bank, sw indian ridge. *Earth and Planetary Science Letters*, 273(1-2):105–114, Aug. 2008. ISSN 0012821X. doi: 10.1016/j.epsl.2008.06.013.
- M. Behn, W. Buck, and I. Sacks. Topographic controls on dike injection in volcanic rift zones. *Earth and Planetary Science Letters*, 246(3-4):188–196, June 2006. doi: 10.1016/j.epsl.2006.04.005.
- M. D. Behn and G. Ito. Magmatic and tectonic extension at mid-ocean ridges: 1. controls on fault characteristics. *Geochemistry, Geophysics, Geosystems*, 9(8):n/a–n/a, Aug. 2008. ISSN 15252027. doi: 10.1029/2008GC001965.
- D. Blackman, J. Karson, and D. Kelley. Geology of the atlantis massif (mid-atlantic ridge, 30 n): Implications for the evolution of an ultramafic oceanic core complex. *Marine Geophysical ...*, 2002.
- D. K. Blackman, J. P. Canales, and A. Harding. Geophysical signatures of oceanic core complexes. *Geophysical Journal International*, 178(2):593–613, 2009. ISSN 0956540X. doi: 10.1111/j.1365-246X.2009.04184.x.
- R. Buck, L. Lavier, and A. Poliakov. Modes of faulting at mid-ocean ridges. *Nature*, 434(7034):719–23, 2005. ISSN 1476-4687. doi: 10.1038/nature03358.
- J. P. Canales, B. E. Tucholke, M. Xu, J. a. Collins, and D. L. DuBois. Seismic evidence for large-scale compositional heterogeneity of oceanic core complexes. *Geochemistry, Geophysics, Geosystems*, 9(8):n/a–n/a, Aug. 2008. ISSN 15252027. doi: 10.1029/2008GC002009.
- S. M. Carbotte, D. K. Smith, M. Cannat, and E. M. Klein. Tectonic and magmatic seg-

mentation of the global ocean ridge system : a synthesis of observations. *Geological Society of London*, 2015.

Y. J. Chen and J. Lin. Mechanisms for the formation of ridge-axis topography at slow-spreading ridges: A lithospheric-plate flexural model. *Geophysical Journal International*, 136:8–18, 1999. ISSN 0956540X. doi: 10.1046/j.1365-246X.1999.00716.x.

E. Choi, L. Lavier, and M. Gurnis. Thermomechanics of mid-ocean ridge segmentation. *Physics of the Earth and Planetary Interiors*, 171(1-4):374–386, Dec. 2008. ISSN 00319201. doi: 10.1016/j.pepi.2008.08.010.

A. Dannowski, I. Grevemeyer, C. R. Ranero, G. Ceuleneer, M. Maia, J. P. Morgan, and P. Gente. Seismic structure of an oceanic core complex at the mid-atlantic ridge, 22 ° 19'n. *Journal of Geophysical Research*, 115(B7):B07106, July 2010. ISSN 0148-0227. doi: 10.1029/2009JB006943.

H. J. B. Dick, M. a. Tivey, and B. E. Tucholke. Plutonic foundation of a slow-spreading ridge segment: Oceanic core complex at kane megamullion, 23 °30'n, 45 °20'w. *Geochemistry, Geophysics, Geosystems*, 9(5):n/a–n/a, May 2008. ISSN 15252027. doi: 10.1029/2007GC001645.

J. Escartín, D. K. Smith, J. Cann, H. Schouten, C. H. Langmuir, and S. Escrig. Central role of detachment faults in accretion of slow-spreading oceanic lithosphere. *Nature*, 455(7214):790–794, 2008. ISSN 0028-0836. doi: 10.1038/nature07333.

C. M. R. Fowler. *The solid earth: an introduction to global geophysics*. Cambridge University Press, 2004.

G. Ito and M. D. Behn. Magmatic and tectonic extension at mid-ocean ridges: 2. origin of axial morphology. *Geochemistry, Geophysics, Geosystems*, 9(9):n/a–n/a, Sept. 2008. ISSN 15252027. doi: 10.1029/2008GC001970. URL <http://doi.wiley.com/10.1029/2008GC001970>.

S. Kirby and A. K. Kronenberg. Rheology of the lithosphere: Selected topics. *Reviews of Geophysics*, 25(6):1219–1244, 1987.

L. L. Lavier, W. R. Buck, and A. N. B. Poliakov. Factors controlling normal fault offset in an ideal brittle layer. *Journal of Geophysical Research*, 105(B10):23431, 2000. doi: 10.1029/2000JB900108.

J. Lin, G. M. Purdy, H. Schouten, J.-C. Sempere, and C. Zervas. Evidence from gravity data for focused magmatic accretion along the Mid-Atlantic Ridge. *Nature*, 344:627–632, 1990. ISSN 0028-0836. doi: 10.1038/344627a0.

C. Mallows and R. C. Searle. A geophysical study of oceanic core complexes and surrounding terrain, mid-atlantic ridge 13 °n-14 °n. *Geochemistry, Geophysics, Geosystems*, 13(6):n/a–n/a, June 2012. ISSN 15252027. doi: 10.1029/2012GC004075.

J.-A. Olive, M. D. Behn, and B. E. Tucholke. The structure of oceanic core complexes controlled by the depth distribution of magma emplacement. *Nature Geoscience*, 3(7): 491–495, June 2010. ISSN 1752-0894. doi: 10.1038/ngeo888.

J.-a. Olive, M. D. Behn, and L. C. Malatesta. Modes of extensional faulting controlled by surface processes. *Geochemistry Geophysics Geosystems*, pages 1–9, 2014. doi: 10.1002/2014GL061507.

T. J. Reston and K. G. McDermott. Successive detachment faults and mantle unroofing at magma-poor rifted margins. *Geology*, 39(11):1071–1074, Oct. 2011. ISSN 0091-7613. doi: 10.1130/G32428.1.

T. J. Reston and C. R. Ranero. The 3-d geometry of detachment faulting at mid-ocean ridges. *Geochemistry, Geophysics, Geosystems*, 12(7):n/a–n/a, July 2011. ISSN 15252027. doi: 10.1029/2011GC003666.

- W. B. F. Ryan, S. M. Carbotte, J. O. Coplan, S. O'Hara, A. Melkonian, R. Arko, R. A. Weissel, V. Ferrini, A. Goodwillie, F. Nitsche, J. Bonczkowski, and R. Zemsky. Global multi-resolution topography synthesis. *Geochemistry, Geophysics, Geosystems*, 10, 2009. ISSN 15252027. doi: 10.1029/2008GC002332.
- H. Schouten, D. K. Smith, J. R. Cann, and J. Escartin. Tectonic versus magmatic extension in the presence of core complexes at slow-spreading ridges from a visualization of faulted seafloor topography. *Geology*, 38(7):615–618, June 2010. ISSN 0091-7613. doi: 10.1130/G30803.1.
- D. K. Smith, H. Schouten, H. J. B. Dick, J. R. Cann, V. Salters, H. R. Marschall, F. Ji, D. Yoerger, A. Sanfilippo, R. Parnell-turner, C. Palmiotto, A. Zhelezov, H. Bai, W. Junkin, B. Urann, S. Dick, M. Sulanowska, P. Lemmond, and S. Curry. Development and evolution of detachment faulting along 50 km of the mid-atlantic ridge near 16.5°n. *Geochemistry Geophysics Geosystems*, pages 4692–4711, 2014. doi: 10.1002/2014GC005563.Received.
- M. Tolstoy, A. J. Harding, and J. A. Orcutt. Crustal Thickness on the Mid-Atlantic Ridge: Bull's-Eye Gravity Anomalies and Focused Accretion. *Science*, 262(October):726–729, 1993. ISSN 0036-8075. doi: 10.1126/science.262.5134.726.
- B. E. Tucholke and J. Lin. A geological model for the structure of ridge segments in slow spreading ocean crust. *Journal of Geophysical Research*, 99(B6):11937, 1994. ISSN 0148-0227. doi: 10.1029/94JB00338.
- B. E. Tucholke, J. Lin, and M. C. Kleinrock. Megamullions and mullion structure defining oceanic metamorphic core complexes on the mid-atlantic ridge, 1998. ISSN 0148-0227.
- B. E. Tucholke, M. D. Behn, W. R. Buck, and J. Lin. Role of melt supply in oceanic de-

tachment faulting and formation of megamullions. *Geology*, 36(6):455, 2008. ISSN 0091-7613. doi: 10.1130/G24639A.1.

D. L. Turcotte and G. Schubert. *Geodynamics*. Cambridge, 2002.

D. L. Whitney, C. Teyssier, P. Rey, and W. R. Buck. Continental and oceanic core complexes. *Geological Society of America Bulletin*, 125(3-4):273–298, Dec. 2012. ISSN 0016-7606. doi: 10.1130/B30754.1.